Monthly Notices of the ROYAL ASTRONOMICAL SOCIETY
MNRAS **500,** 2666–2684 (2021) doi:10.1093/mnras/staa3320

Coronal-line forest active galactic nuclei – I. Physical properties of the emission-line regions

F. C. Cerqueira-Campos [1]★ A. Rodríguez-Ardila,[1,2]★† R. Riffel [3] M. Marinello,[2] A. Prieto[4] and L. G. Dahmer-Hahn[2]

[1]*Divisão de Astrofísica, Instituto Nacional de Pesquisas Espaciais, Avenida dos Astronautas 1758, São José dos Campos, 12227-010, SP, Brazil*
[2]*Laboratório Nacional de Astrofísica - Rua dos Estados Unidos 154, Bairro das Nações. CEP 37504-364, Itajubá, MG, Brazil*
[3]*Departamento de Astronomia, Instituto de Física, Universidade Federal do Rio Grande do Sul, Av. Bento Gonçalves 9500, Porto Alegre, RS, Brazil*
[4]*Instituto de Astrofísica de Canarias, C/ Via Láctea, S/N, San Cristobal de La Laguna, Tenerife, Spain*

Accepted 2020 October 20. Received 2020 August 29; in original form 2020 February 17

ABSTRACT

Coronal-line forest (CLiF) active galactic nuclei (AGNs) are characterized by strong high-ionization lines, which contrasts with what is found in most AGNs. Here, we carry out a multiwavelength analysis aimed at understanding the physical processes in the narrow-line region (NLR) of these objects, and at discovering whether they are indeed a special class of AGNs. By comparing coronal emission-line ratios we conclude that there are no differences between CLiF and non-CLiF AGNs. We derive physical conditions of the NLR gas and we find electron densities in the range of 3.6×10^2 to 1.7×10^4 cm^{-3} and temperatures of 3.7×10^3 to 6.3×10^4 K, suggesting that the ionization mechanism is associated primarily with photoionization by the AGN. We suggest an NLR dominated by matter-bounded clouds to explain the high-ionization line spectrum observed. The mass of the central black hole, derived from the stellar velocity dispersion, shows that most of the objects have values in the interval 10^7–10^8 M$_\odot$. Our results imply that CLiF AGNs are not in a separate category of AGNs. In all optical/near-infrared emission-line properties analysed, they represent an extension to the low/high ends of the distribution within the AGN class.

Key words: galaxies: active – galaxies: Seyfert – infrared: galaxies.

1 INTRODUCTION

Coronal lines (CLs), or forbidden high-ionization emission lines (FHILs), originate from forbidden fine structure transitions excited by collisions in highly ionized species (ionization potential, IP $\geq$ 100 eV). Because of their very high IP, they are considered to be a reliable signature of the presence of an active galactic nucleus (AGN) in galaxies (Penston et al. 1984; Prieto & Viegas 2000; Prieto, García & Espinosa 2002; Reunanen, Kotilainen & Prieto 2003; Satyapal et al. 2008; Goulding & Alexander 2009). However, they are also produced in supernova remnants (SNRs; Oliva et al. 1999; Smith et al. 2009), planetary nebulae (Pottasch, Bernard-Salas & Roellig 2009) and Wolf–Rayet stars (Schaerer & Stasinska 1999). Typical CL luminosities in these latter objects are low, $\sim 10^{31}-10^{33}$ erg s^{-1} (Dopita et al. 2018). Thus, several thousands of these might be necessary to produce detectable CL emission if an AGN origin is ruled out, in which case the sources need to be forming stars very actively. Moreover, in SNRs, CLs vary strongly with time. Komossa et al. (2008, 2009) and Wang et al. (2011) have shown that, in these objects, they fade on time-scales of a few years.

The presence of CLs in the spectra of AGNs is attributed to the existence of highly energetic processes associated with nuclear activity. Some of these lines are conspicuous and their emission region can be extended to scales of up to a few hundred parsec (Prieto, Marco & Gallimore 2005; Rodríguez-Ardila et al. 2006; Mazzalay, Rodríguez-Ardila & Komossa 2010; Müller-Sánchez et al. 2011). Usually, [Ne V] λ3435 Å (IP = 100 eV) and [Fe VII] λ6087 Å (IP = 100 eV) are the most prominent CLs in the optical region (Murayama & Taniguchi 1998) while [Si VI] 1.963 μm (IP = 166 eV) is the strongest CL in the near-infrared (NIR). However, CLs up to $\chi = 505$ eV ([S XII] λ7609 Å) have been reported in AGNs (Mazzalay et al. 2010). The observed luminosities of such lines cover about three orders of magnitude, from 10^{38} up to 10^{41} erg s^{-1} (Rodríguez-Ardila et al. 2011).

Although CLs are frequent in AGN spectra, not all AGNs display them. Riffel, Rodríguez-Ardila & Pastoriza (2006), using a sample of 47 AGNs in the NIR, found that in 67 per cent of the objects, one CL is identified. They showed that the lack of CLs in the remaining 33 per cent of objects is genuine and not driven by sensitivity detection issues. In their analysis, the faintest [Si VI] coronal luminosity was $\sim 10^{38}$ erg s^{-1}, measured in NGC 4051 at a redshift $z = 0.00234$. More distant sources, such as Ark 564 ($z = 0.0247$) or PG 1448+273 ($z = 0.065$) display a [Si VI] luminosity nearly 2 dex higher. All objects were observed with a similar signal-to-noise ratio (S/N). Similar results are also found by Lamperti et al. (2017). In the optical region, CLs of iron (i.e. [Fe VII] and [Fe X]) are usually observed, but no quantitative studies of its frequency have been made yet.

★ E-mail: fernando.campos@inpe.br (FCCC); aardila@lna.br (ARA)
† Visiting Astronomer at the Infrared Telescope Facility, which is operated by the University of Hawaii under contract NNH14CK55B with the National Aeronautics and Space Administration.

Table 1. Sample of CLiF AGNs as defined by Rose et al. (2015a) and employed in this work. Column 9 lists the classification into AGNs of Type I or II accoris correctding to Rose et al. (2015b) while the last column lists the classification based on results obtained from this work (see Section 4.1).

Galaxy	Redshift (z)	Telescope/instrument	Date (yyyy.mm.dd)	$E(B-V)_G$ (mag)	Airmass	Exp. time (s)	PA° (E of N)	Classification (Rose et al. 2015b)	Classification (this work)
(1)	(2)	(3)	(4)	(5)	(6)	(7)	(8)	(9)	(10)
ESO138–G001	0.0091	SOAR/Goodman	2017.03.11	0.176	1.13	3 × 900	279	Type II	Type I
		Blanco/ARCoIRIS	2017.04.07		1.16	16 × 180	0.0		
SDSS J164+43	0.2210	Gemini/GNIRS	2017.02.15	0.01	1.24	16 × 180	90	Type II	Type I
III Zw 77	0.0342	IRTF/SpeX	2015.04.12	0.09	1.08	18 × 180	338	Type I	Type I
MRK 1388	0.0213	IRTF/SpeX	2015.05.04	0.03	1.00	8 × 200	300	Type II	Type I
SDSS J124+44	0.0420	...	...	0.02	...	...	...	Type II	Type II
2MASX J113+16	0.1740	Gemini/GNIRS	2017.02.20	0.03	1.25	12 × 160	90	Type II	Type I
NGC 424	0.0118	SOAR/Goodman	2014.08.07	0.01	1.02	4 × 900	60	Type II	Type I
		Blanco/ARCoIRIS	2016.09.19		1.02	12 × 180	270		

Despite its importance, these lines tend to be weak. [Fe VII] 6087 Å, which is the brightest CL in the 3500–7500 Å region, is usually 1–10 per cent of the strength of [O III] 5007 Å (Murayama & Taniguchi 1998).

Recently, a new class of AGNs, called coronal-line forest (CLiF) AGNs, have been introduced in the literature (Rose, Elvis & Tadhunter 2015a; Rose et al. 2015b; Glidden et al. 2016). Among several interesting properties, CLiF AGNs are characterized by: (i) the emission-line flux ratio [Fe VII] $\lambda6087/H\beta > 0.25$; (ii) [Fe X] $\lambda6374/H\beta > 0.2$; (iii) [Ne V] $\lambda3426/H\beta > 1$; (iv) the fact that CLs are not blueshifted with respect to the low-ionization lines ($\Delta v \lesssim 100$ km s^{-1}); (v) the fact that the velocity widths of CLs are narrow and similar to those of low-ionization lines (FWHM < 300 km s^{-1}) using single Gaussian fits. Optical luminosities of these CLs are found to be between 10^{40} and 10^{41} erg s^{-1} (see Section 4.4). These values are well within the interval of the CL luminosities reported by Gelbord, Mullaney & Ward (2009) in a sample 63 AGNs.

Another peculiar characteristic identified by Rose et al. (2015a, hereafter RET15) in CLiF AGNs is the high value of the Hα/Hβ ratio, which in all objects studied was between 3.8 and 6.6 (taking into account the limits of the error bars). This is higher than the Balmer decrement assuming case B for low-density gas. They interpreted this result as due to high-density gas in the narrow-line region (NLR) instead of being attributed to dust extinction because the values found for Hγ/Hβ are consistent with the intrinsic case B value of 0.47 (Osterbrock & Ferland 2006).

The results obtained by RET15 suggest that most of the Hα emission is produced in the same region of the coronal-line forest, enhancing the flux ratio Hα/Hβ. The gas density they obtained by modelling the NLR is in the range $10^6-10^{7.5}$ cm^{-3}, much higher than that expected for typical NLR conditions ($<10^4$ cm^{-3}; Osterbrock & Ferland 2006).

RET15 classified only seven CLiF AGNs from an initial sample of ∼5000 AGN spectra from the Sloan Digital Sky Survery (SDSS).

Here, we carry out the first NIR study of CLiF AGNs in the literature along with a re-analysis of the optical spectra of these objects. We detail in Section 2 the sample and observations. Our additional data widen the number and species of CLs suitable to derive the physical conditions of the CL region anis correctd NLR in these interesting sources (Sections 3 and 4). Stellar and gas kinematics properties are derived in Section 5. We also derive additional properties of CLiF AGNs, such as the mass of the supermassive black hole (SMBH), in order to construct a more complete picture of these sources. Our main conclusions are drawn in Section 6.

2 SAMPLE, OBSERVATIONS AND DATA REDUCTION

The sample chosen for this analysis consists of the seven CLiF AGNs already identified by RET15, observed using optical ($3400 \leq \lambda \leq 7500$ Å) and NIR ($7800 \leq \lambda \leq 25000$ Å) spectroscopy. Table 1 lists the basic properties of the objects as well as the log of observations. Details about telescope set-up and data reduction according to the wavelength interval are given below. Note that we did not collect optical spectra for 2MASX J113111.05+162739 or NIR spectra for SDSS J124134.25+442639.2.

2.1 Optical spectroscopy

Optical spectra for SDSS J124134.25+442639.2, MRK 1388, III Zw 77 and SDSS J164126.91+432121.5 were obtained from the SDSS Data Release 7 (DR7) data base (Abazajian et al. 2009). These spectra have already been published by RET15. Below, we detail the observations and data reduction procedure for ESO 138–G001 and NGC 424.

2.1.1 Goodman/SOAR observations

Optical spectra of ESO 138–G001 and NGC 424 were obtained with the 4.1-m Southern Observatory for Astrophysical Research (SOAR) Telescope at Cerro Pachon, Chile. The observations were carried out using the Goodman spectrograph (Clemens, Crain & Anderson 2004), equipped with a 400 l mm^{-1} grating and a 0.8-arcsec slit width, giving a resolution $R \sim 1500$. In addition to the science frames, standard stars (Baldwin & Stone 1984) were observed for flux calibration. HgAr arc lamps were taken after the science frames for wavelength calibration. Daytime calibrations include bias and flat-field images.

The data were reduced using standard IRAF[1] tasks, including subtraction of the bias level and division of the science and flux standard star frames by a normalized master flat-field image. Thereafter, the spectra were wavelength-calibrated by applying the dispersion solution obtained from the arc lamp frames. Finally, the spectra of standard stars were extracted and combined to derive the sensitivity function, later applied to the science one-dimensional (1D) spectra. The final products are wavelength- and flux-calibrated optical spectra.

[1] IRAF is distributed by the National Optical Astronomy Observatories, which are operated by the Association of Universities for Research in Astronomy, Inc., under cooperative agreement with the National Science Foundation.

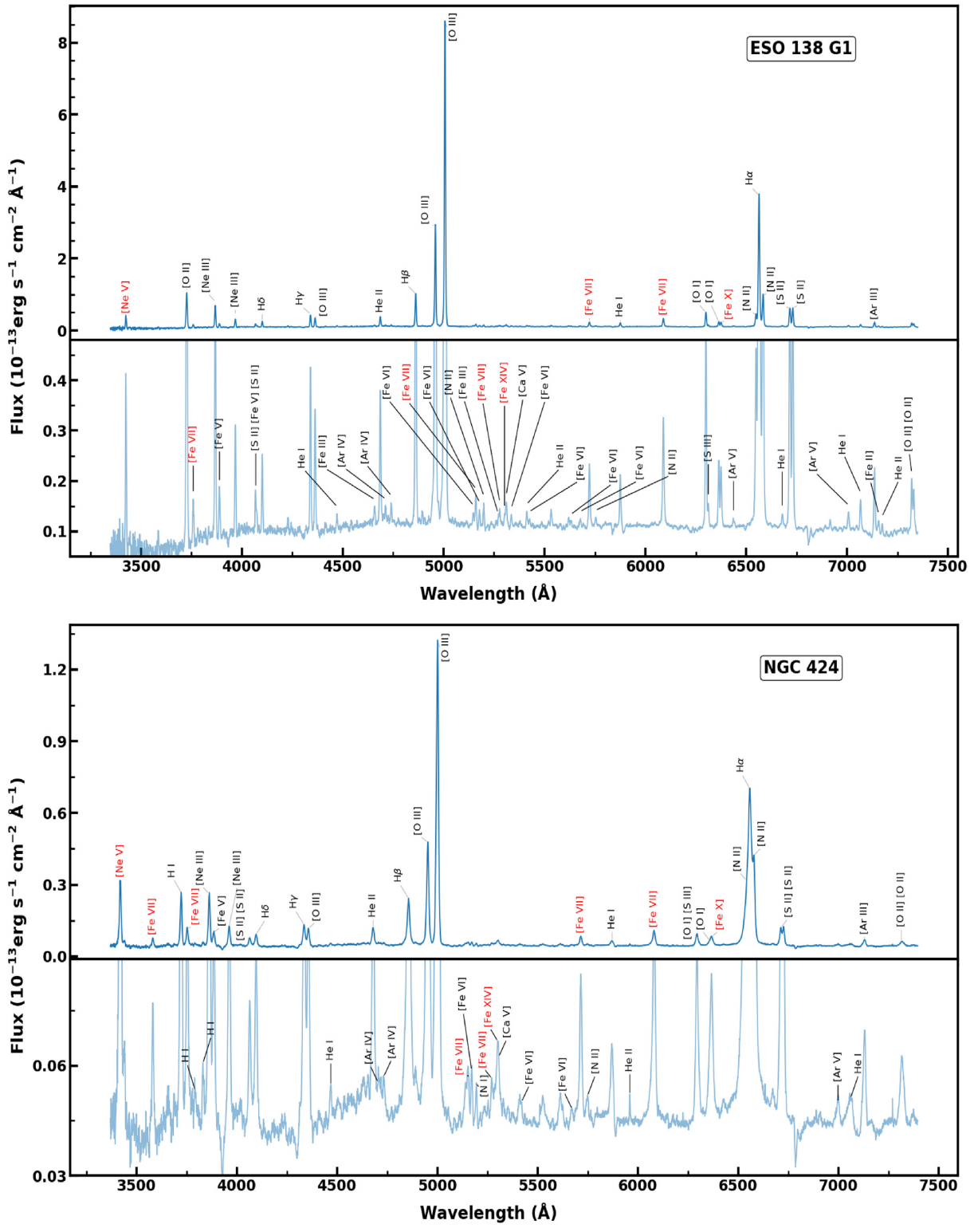

Figure 1. Optical spectra obtained by Goodman/SOAR. In the bottom panel, for both spectra, a zoom around the continuum level is displayed to show the faintest lines identified. The ions belonging to CL transitions are given in red.

In all cases above, the final spectra were corrected for Galactic extinction using the extinction maps of Schlafly & Finkbeiner (2011) (see column 6 of Table 1) and the Cardelli, Clayton & Mathis (1989) law. The final reduced spectra are shown in Fig. 1.

2.2 NIR spectroscopy

The NIR spectra of the sample listed in Table 1 were obtained at three different observatories: Cerro Tololo Inter-American Observatory (CTIO), Gemini North and the NASA Infrared Telescope Facility

(IRTF). In all cases, a cross-dispersed spectrograph, providing simultaneous coverage of the 0.8–2.4 μm region was employed. Below, we provide basic descriptions of the observations and data reduction procedure for each set of data.

2.2.1 *GNIRS/Gemini spectroscopy*

The NIR spectra of SDSS J124134.25+442639.2 and SDSS J164126.91+432121.5 were obtained in queue mode with the 8.1-m Gemini North telescope atop Mauna Kea (Program ID = GN2017A-Q40). The Gemini NIR spectrograph (GNIRS; Elias et al. 2006) in the cross-dispersed mode was employed. It allows simultaneous $z + J$-, H- and K-band observations, covering the spectral range $0.8 - 2.5$ μm in a single exposure. The GNIRS science detector consists of an ALADDIN 1k × 1k InSb array. The instrument set-up includes a 32 l mm^{-1} grating and a 0.8 × 7 arcsec slit, giving a spectral resolution of $R \sim 1300$ (or 320 km s^{-1} FWHM). Individual exposures were taken, nodding the source in a ABBA pattern along the slit. Right after the observation of the science frames, an A0 V star was observed at a similar airmass, with the purpose of flux calibration and telluric correction.

The NIR data were reduced using the XDGNIRS pipeline (v2.0),[2] which delivers a full reduced, wavelength- and flux-calibrated, 1D spectrum with all orders combined (Mason et al. 2015). Briefly, the pipeline cleans the two-dimensional (2D) images from radiative events and prepares a master flat constructed from quartz IR lamps to remove pixel-to-pixel variation. Thereafter, the s-distortion solution is obtained from daytime pinhole flats and applied to the science and telluric images to rectify them. Argon lamp images are then used to find the wavelength dispersion solution, followed by the extraction of 1D spectra from the combined individual exposures. The telluric features from the science spectrum are removed using the spectrum of an A0 V star. Finally, the flux calibration is achieved assuming a blackbody shape for the standard star (Pecaut & Mamajek 2013) scaled to its K-band magnitude (Skrutskie et al. 2006). The different orders are combined in a single 1D spectrum and corrected for Galactic extinction using the Cardelli et al. (1989) law and the extinction maps of Schlafly & Finkbeiner (2011). The spectra are shown in Fig. 2.

2.2.2 *IRTF/SpeX data*

NIR spectra of III Zw 77 and Mrk 1388 were obtained at the NASA 3-m IRTF using the SpeX spectrograph (Rayner et al. 2003) in the short cross-dispersed mode (SXD; 0.7–2.4 μm). The detector consists of a Teledyne 2048 × 2048 Hawaii-2RG array with a spatial scale of 0.10 arcsec pixel–1. A slit of 0.8 arcsec x 15 arcsec, providing a spectral resolution, on average, of 320 km s^{-1}, was employed.

Observations were carried out nodding in two positions along the slit. Right before or after the science target, a telluric star, close in airmass to the former, was observed in order to remove telluric features and to perform the flux calibration. CuHgAr frames were also observed at the same position as the galaxies for wavelength calibration. The spectral reduction, extraction and wavelength calibration procedures were performed using SPEXTOOL V4.1, an IDL-based software developed and provided by the SpeX team for the IRTF community (Cushing, Vacca & Rayner 2004). The removal of telluric features and flux calibration were done using XTELLCOR (Vacca, Cushing & Rayner 2003), another software package available from the SpeX team. The different orders were merged into a single 1D spectrum from 0.7 to 2.4 μm using the XMERGEORDERS routine. After this procedure, the IDL routine XLIGHTLOSS, also written by the SpeX team, was employed. It corrects an input spectrum for slit losses relative to the standard star used for flux calibration. This program is useful if either the object or the standard star were not observed with the slit at the parallactic angle. Differential refraction is, indeed, the main source of uncertainty in flux calibration and it was minimized following the above procedure. Finally, the spectra were corrected for Galactic extinction using the Cardelli et al. (1989) law and the extinction maps of Schlafly & Finkbeiner (2011). The spectra are shown in Fig. 3.

2.2.3 *Blanco/ARCoIRIS data*

The NIR spectra of ESO 138–G001 and NGC 424 were obtained using the ARCoIRIS spectrograph attached to the 4.1-m Blanco Telescope (Schlawin et al. 2014). The science detector employed is a 2048 × 2048 Hawaii-2RG HgCdTe array with a sampling of 0.41 arcsec pixel^{-1}. The slit assembly is 1.1 arcsec wide and 28 arcsec long. The delivered spectral resolution R is ∼3500 across the six science orders. Similar to the IRTF/SpeX data, telluric standards were observed close to the science targets to warrant good telluric band cancellations and flux calibration.

Data reduction was carried out using SPEXTOOL v4.1 with some modifications specifically designed for the data format and characteristics of ARCoIRIS. The procedure follows the same steps and recipes as for SpeX. The final data product consist of a 1D spectrum, wavelength- and flux-calibrated with all individual orders merged to form a continuous 0.9–2.4 μm spectrum. We then corrected these data for Galactic extinction using the Cardelli et al. (1989) law and the extinction maps of Schlafly & Finkbeiner (2011).

In order to verify the quality of the flux calibrations in the NIR spectra, we compared our data with the Two-Micron All-Sky Survey (2MASS) photometric points. The only data that required a calibration adjustment were those taken with ARCoIRIS (ESO 138–G001 and NGC 424). In order to rescale the flux level to that of the 2MASS, a third-degree polynomial function was applied using the Python LMFIT routine (Newville et al. 2016). The spectra are shown in Fig. 4.

3 CONTINUUM EMISSION ANALYSIS

In this section, we describe the modelling of the continuum emission in the optical and NIR in order to remove the effects of both the underlying stellar population of the host galaxy and the continuum emission attributed to dust heated by the AGN. The first component is observed in both spectral regions while the second is restricted to the NIR.

3.1 Optical continuum

A rapid inspection of the optical spectra of the CLiF sample (see fig. 1 of RET15 and Fig. 1 in this paper) reveals the presence of strong absorption lines, showing evidence of the contribution of the stellar population from the host galaxy to the observed integrated spectra. It is not of interest in this paper to study the stellar population, but to model and subtract this contribution to obtain suitable flux measurements for the gas in the central region. This procedure

[2]Based on the Gemini IRAF packages

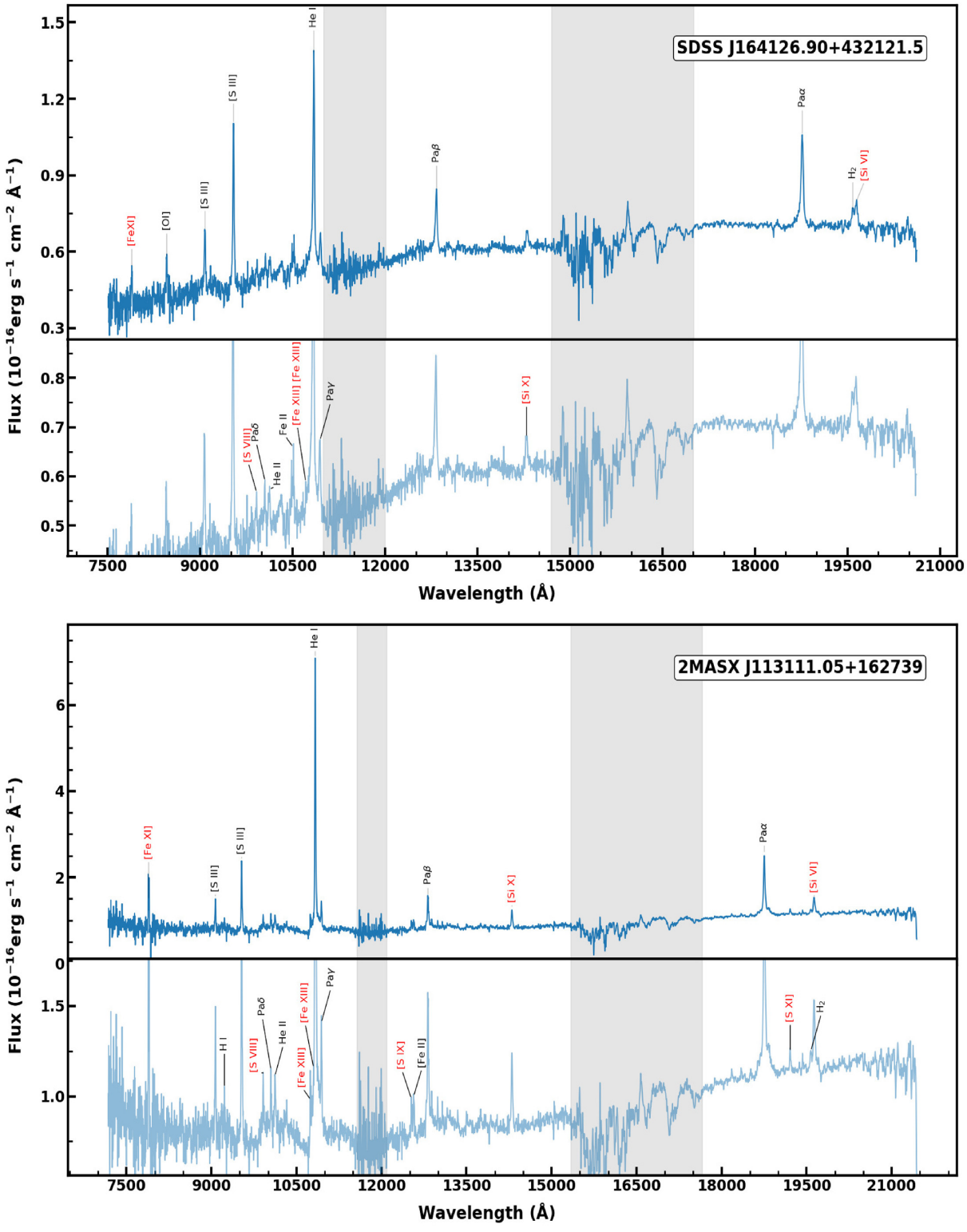

Figure 2. NIR spectra obtained by GNIRS/Gemini. The shaded area represents the region of low atmospheric transmission. Lines located in these regions were not employed in the analysis. In the bottom panel, for both spectra, a zoom is displayed to identify the faintest lines. CLs are identified with red labels.

particularly affects the measurements of the Balmer decrement and the flux of lines that are partially absorbed by the stellar continuum.

In order to remove the stellar contribution, we used the penalized pixel-fitting (pPXF) software developed by Cappellari & Emsellem (2004) and updated by Cappellari (2017). This routine uses maximum penalized likelihood estimation with the principle of searching for the best spectral fit by combining stellar spectra from a library of simple stellar populations. Here, the templates that were used to generate the pPXF fits are those of Bruzual & Charlot (2003). Fig. 5 shows

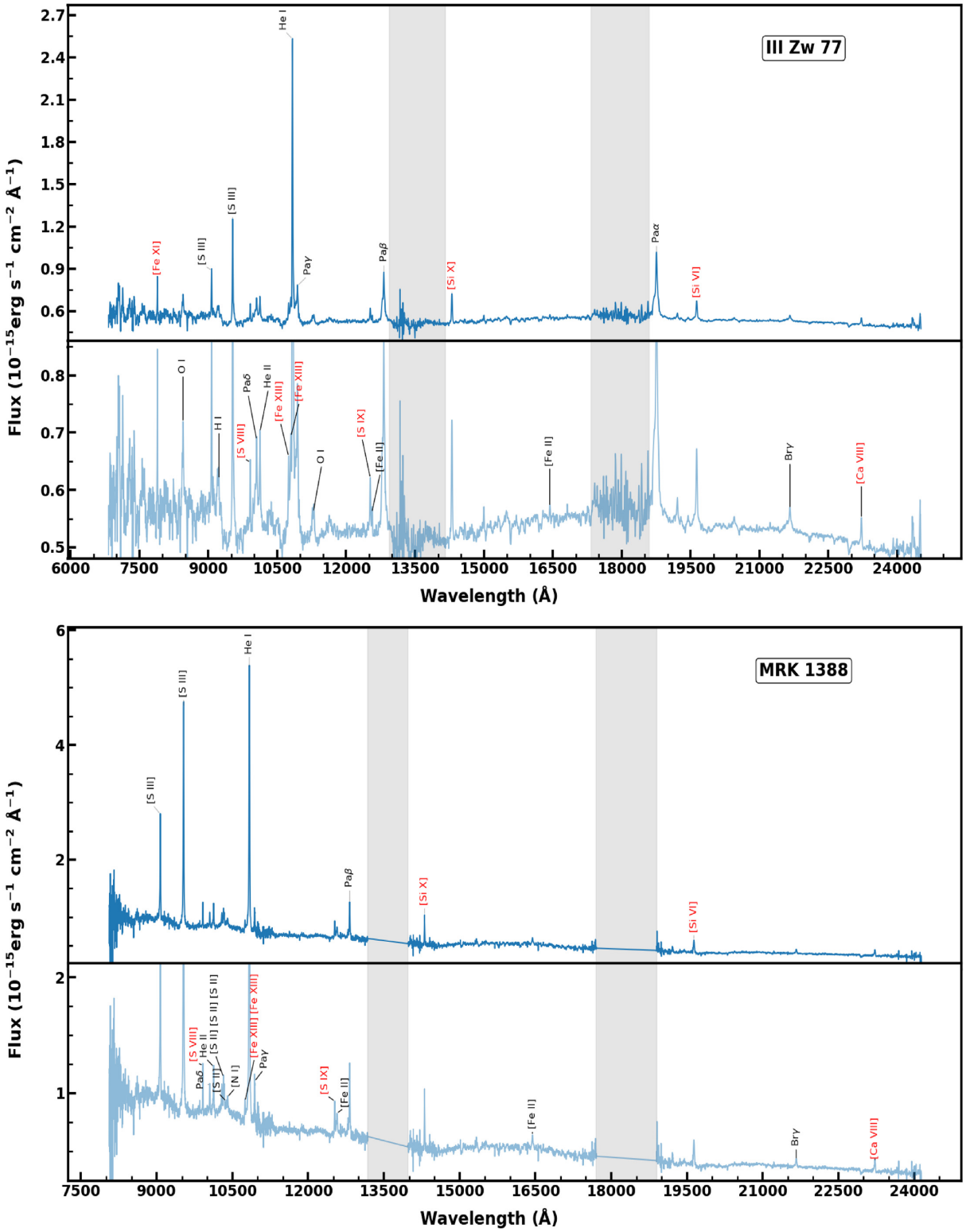

Figure 3. Same as Fig. 2 but for the IRTF/SpeX spectra.

the fits carried out for the galaxy sample and the resulting nebular emission after subtraction of the stellar component. In addition, pPXF also estimates the stellar velocity dispersion, which will be employed in the determination of the mass of the black hole (see Section 5.2).

3.2 NIR continuum

Accepting the unified model to describe the different types of AGNs, the presence of a dusty torus leaves a spectroscopic signature that starts to show up in the NIR. Dust absorbs a fraction of the

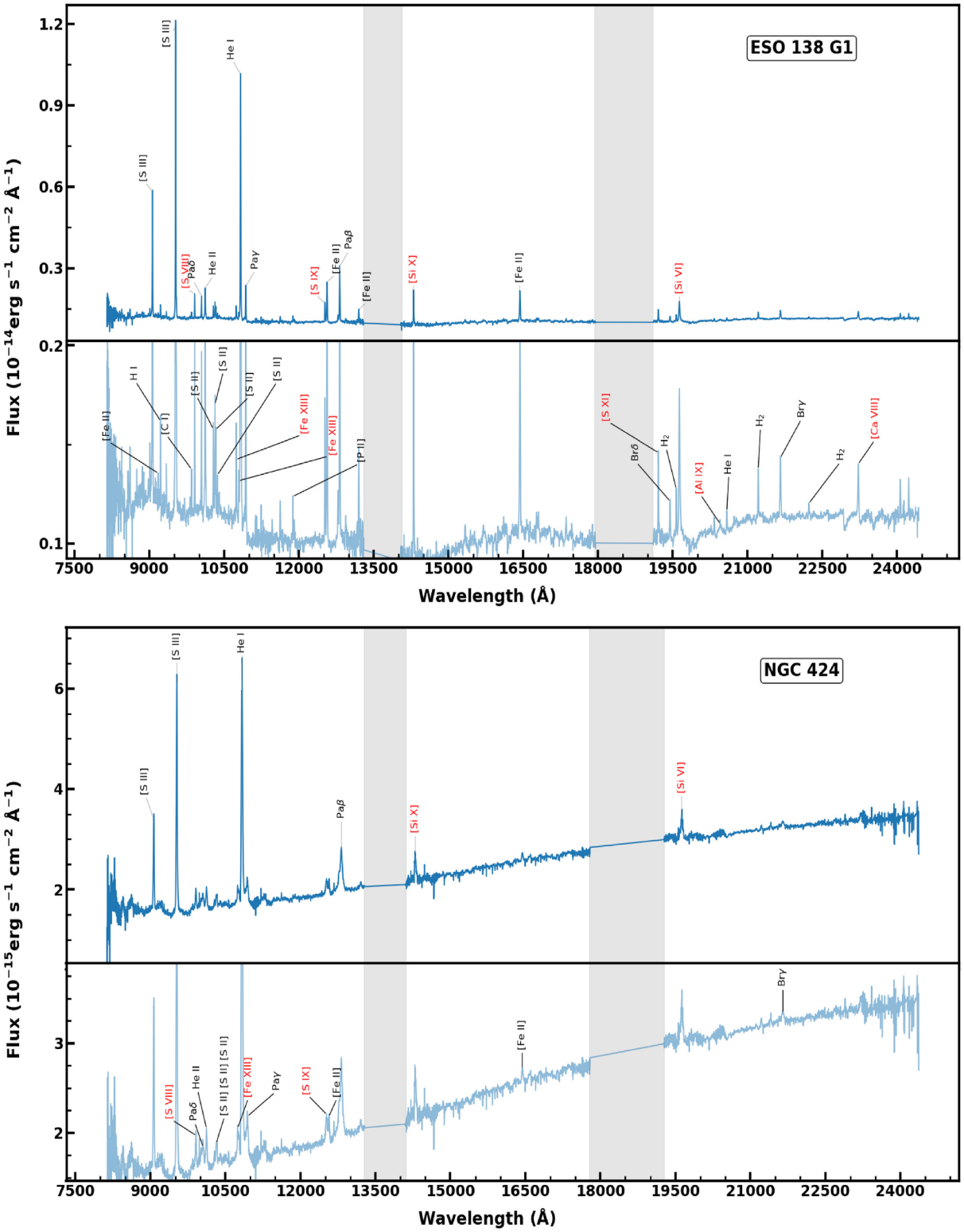

Figure 4. Same as Fig. 2 but for the Blanco/ARCoIRIS spectra.

optical/ultraviolet continuum from the central source and radiates it back at longer wavelengths, from 1 μm up to the far-infrared.

Observational evidence corroborates models describing the NIR continuum in AGNs from 1 to 10 μm as being predominantly or entirely dominated by hot dust (Edelson & Malkan 1986; Barvainis 1987).

Rodríguez-Ardila & Mazzalay (2006) confirmed this scenario in the Seyfert 1 AGN Mrk 1239 by adjusting the excess of the NIR continuum over the power law extrapolated from the optical region, as due to dust emission. They employed a simple blackbody function at a temperature of 1200 K. This is close to the sublimation temperature of dust grains (∼1500 K).

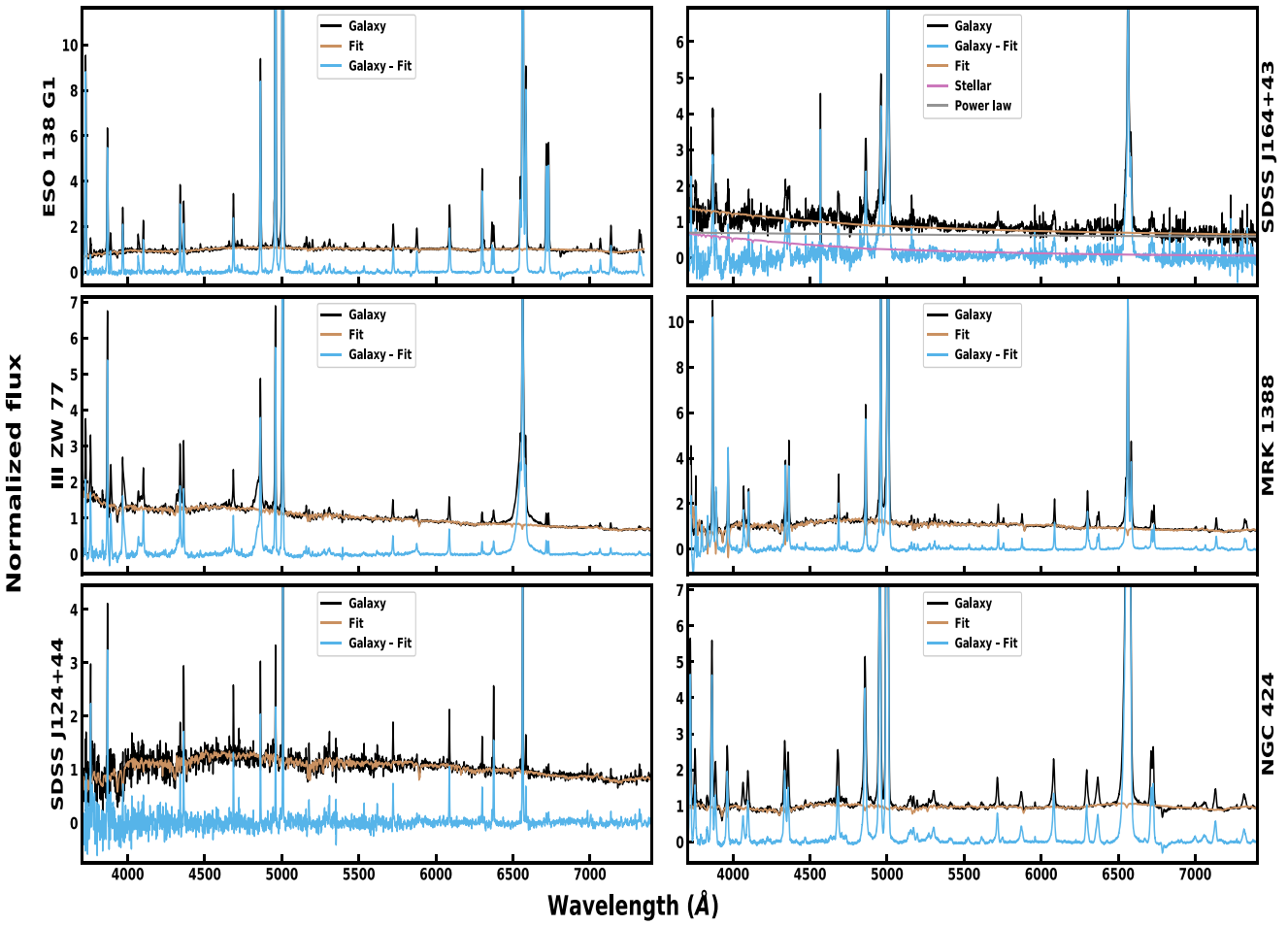

Figure 5. Modelling of the stellar contribution for CLiF AGNs in the optical region. In all panels, the observed spectrum is in black, the stellar continuum is in red and the nebular emission obtained after subtraction of the stellar continuum is in blue.

Thus, to fit the continuum of our sample of CLiF AGNs in the NIR, in addition to the stellar population templates, a function that represents the hot dust emission should be employed. For the former component, the IRTF library of stellar spectra (Rayner, Cushing & Vacca 2009) was used to fit the data. It is composed of 296 spectra in the wavelength range 0.8–5.0 μm, with a resolving power of approximately 2000. The SpeX/IRTF spectrograph was used for the observation of that library.

For the latter component, blackbody templates at the temperatures of 700, 1000, 1300 and 1500 K were included following the procedure outlined in Riffel et al. (2009). Dust emission at that temperature interval is expected for the innermost region of the torus and should leave a spectroscopic signature in the form of an excess of continuum emission over the power law, peaking at about 2 μm. The results are shown in Fig. 6. It can be seen that except in SDSS J164+43, where no evidence of stellar population was found, the NIR continuum consists of the contribution of stellar light plus the hot dust component.

4 MEASUREMENT OF THE EMISSION-LINE FLUX

After subtraction of the stellar and hot dust contribution, the resulting spectra consist of emission lines produced by the gas from the nuclear and circumnuclear regions of the galaxies. In order to measure the flux of the lines, we modelled the observed profiles with a suitable function that best represents them and then integrated the flux under that function. For this purpose, we employ the LINER routine (Pogge & Owen 1993). This software performs a least-squares fit of a model line profile (Gaussian, Lorentzian or Voight functions) to a given line or set of blended lines to determine the flux, peak position and FWHM of the individual components. Typically, one or two Gaussian components were necessary to represent the NLR lines. For permitted lines with a clear broad component associated with the BLR, a third Gaussian function was added. Figs 7–11 show examples of the deblending procedure carried out for the most important emission lines in the sample. Tables A1–A6 and B1−B6 in the online appendices list the peak position (column 2), ionization potential (IP, column 3), FWHM (column 4) and integrated flux (column 5) measured for all lines identified in each CLiF AGN, in both the optical and the NIR.

4.1 Detection of hidden broad lines in Type II CLiF AGNs

Rose et al. (2015b) employed the colour index [*W*2–*W*4] derived from the *Wide-field Infrared Survey Explorer* (*WISE*) to verify the inclination angle of the torus relative to the observer. From their analysis, they found that the [*W*2–*W*4] index in CLiF AGNs was

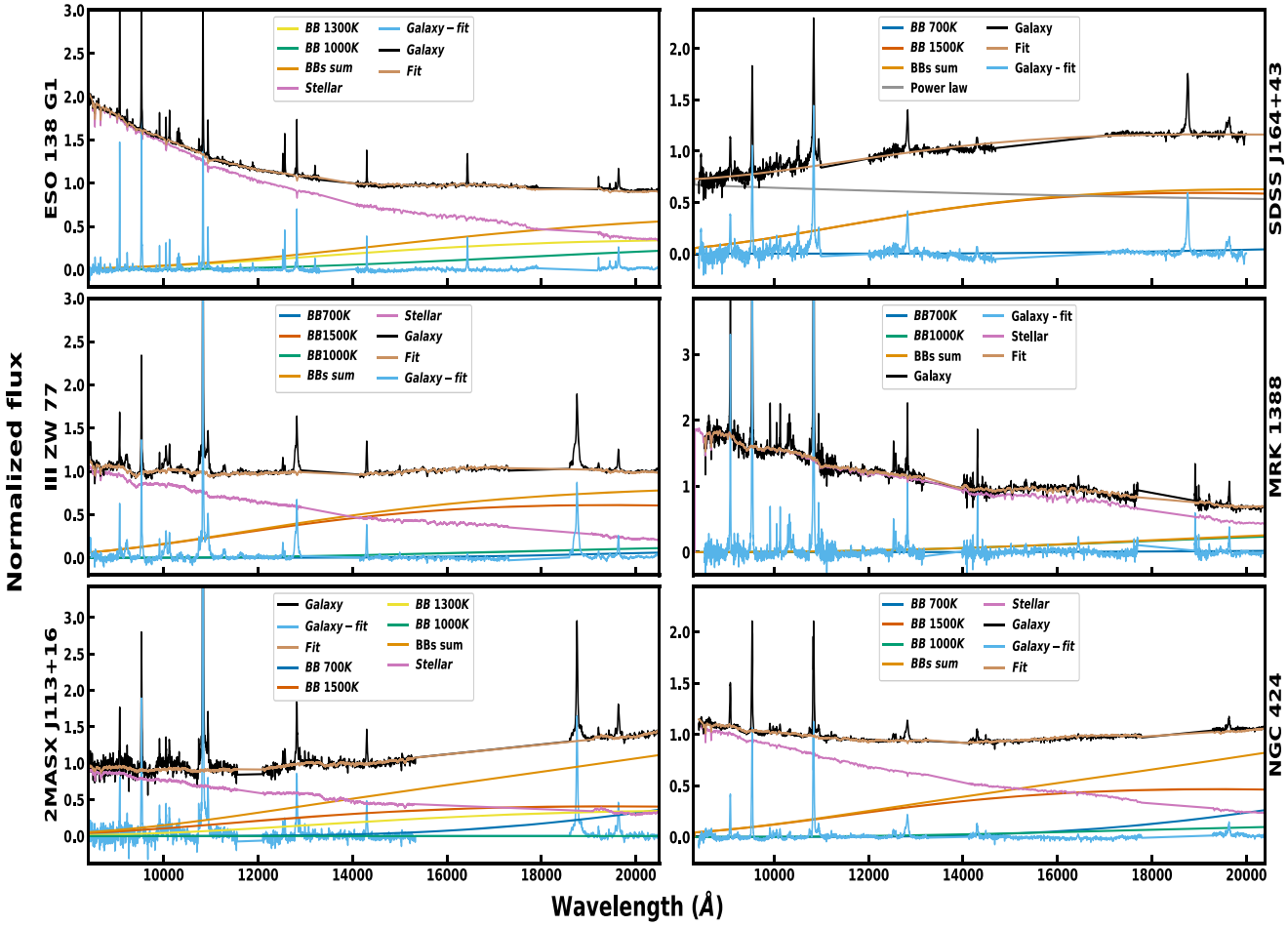

Figure 6. Fits of the continuum emission in the NIR. In all panels, the observed spectrum is in black, the stellar template in magenta and the hot dust in orange. After subtraction of the continuum contribution, the residual consists of the nebular gas emission, shown in cyan.

intermediate between objects classified as Type I and Type II AGNs. This result was consistent with the hypothesis that the torus in CLiF AGNs is observed at intermediate inclination angles. However, as can be seen in the last column of Table 1, only one out of the seven CLiF AGNs is a genuine Type II object. In most targets, broad components in the permitted lines were observed, even in those objects previously classified as Type II AGNs. This result shows that the majority of CLiF AGNs are indeed Type I AGNs.

The classification of MRK 1388 is ambiguous. It displays a broad component in the Balmer lines with FWHM of 1040 km s^{-1}. This would tentatively classify it as a narrow-line Seyfert 1 (NLS1). However, a similar broad component is also detected (in blueshift) in the [O III] lines (see Fig. 11), which suggests the presence of an outflow rather than a genuine BLR. Previously, Doi (2015) classified MRK 1388 as an NLS1 because of the strong featureless continuum observed in that source, although the optical spectrum does not display evidence of broad components in the permitted lines. He suggested that this galaxy has a heavily obscured BLR.

Regarding our NIR spectrum of MRK 1388, a similar broad component as the one detected in [O III] is also found in [S III] (see Table B4). It suggests that this object, indeed, displays evidence of an outflow. Notice that no broad NIR H I line was found. As the optical and NIR spectra are not contemporaneous, it is possible that variability between both sets of data might explain the lack of a broad H I component in the NIR. Reports of such extreme variability are frequently found in the literature and are exemplified by so-called changing-look AGNs. These objects show extreme changes of emission-line intensities, with sometimes almost complete disappearance and reappearance of the broad component (e.g. Lyutyj, Oknyanskij & Chuvaev 1984; Kollatschny & Fricke 1985; Denney et al. 2014; Oknyansky et al. 2019). Although the variability of CLs has been detected previously in some sources (e.g. Landt et al. 2015a, b), the results show that they vary differently as the permitted lines.

In the light of the evidence presented above, we keep the classification of MRK 1388 as an NLS1 galaxy.

In summary, the optical and NIR spectroscopy presented here reveal that just one (SDSS J124+44) out of the seven CLiF AGNs displays spectral characteristics typical of Type II objects. This is at odds with the model presented in Glidden et al. (2016) to explain CLiF AGNs, as it applies only to sources optically classified as Type II.

4.2 Extinction of the NLR in CLiFs

In their optical study of CLiF AGNs, RET15 found that the deviation from the intrinsic Balmer decrement Hα/Hβ = 3.1 derived for their sample was attributed to high-density gas in the region where the Hα line is formed. However, the lack of subtraction of the stellar

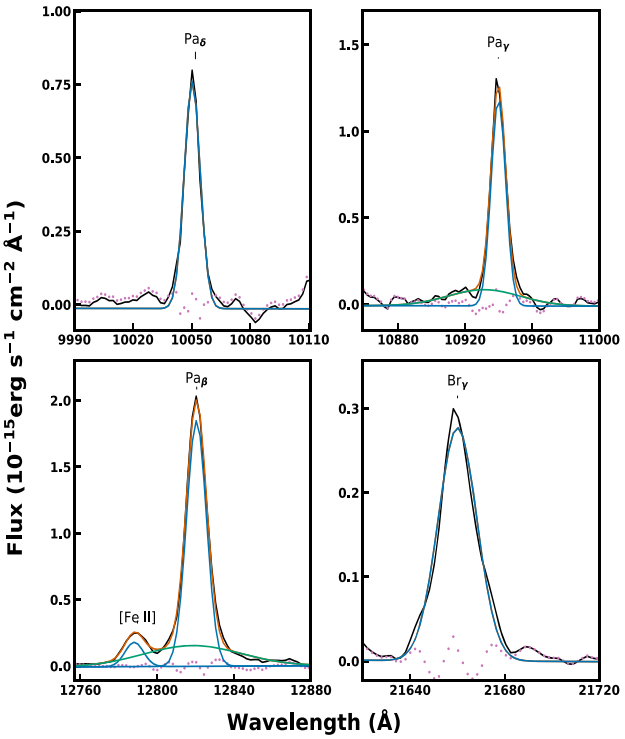

Figure 7. Multicomponent Gaussian fit for the NIR of some H I lines in the CLiF AGN ESO 138–G001. In each panel, observations are in black, narrow components in blue, broad components in green and the total fit in red. The magenta dotted line shows the residuals after subtracting the total fit. It is possible to notice that the broad component is hidden for the less intense hydrogen lines.

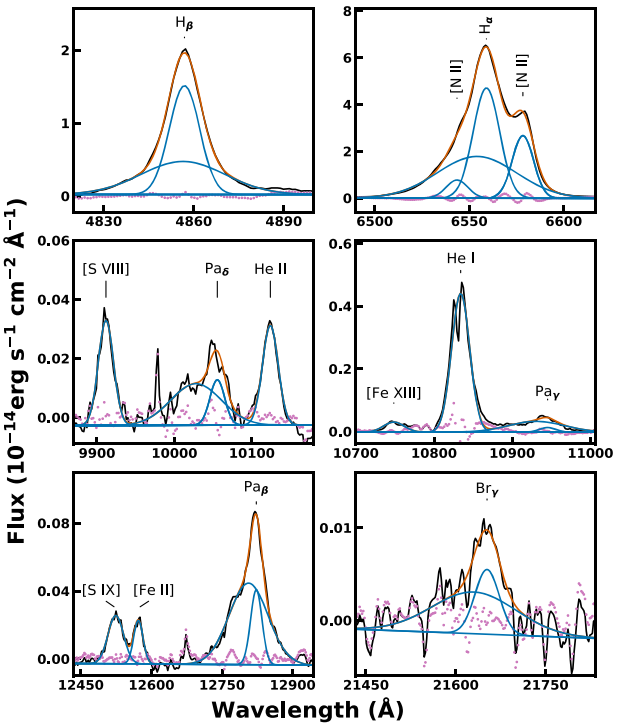

Figure 8. Multicomponent Gaussian fit for the optical and NIR regions around the H I lines in the CLiF AGN NGC 424. In each panel, observations are in black, individual components in blue, and the total fit in red. The magenta dotted line shows the residuals after subtracting the total fit.

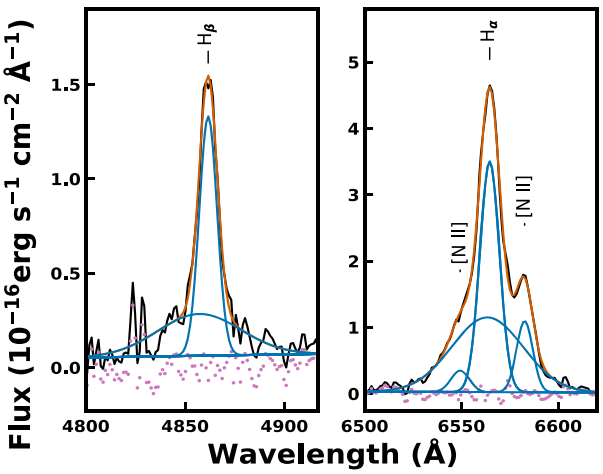

Figure 9. Same as Fig. 8 but for Hβ (left panel) and Hα (right panel) observed in SDSS J164126.91+432121.

continuum may hide part of the Hβ emission. This is because part of the line is within the absorption dip produced by the stellar population. As a result, the line ratio Hα/Hβ is overestimated relative to their theoretical value, even in the absence of dust extinction.

In this work, because of the increase in the wavelength coverage by including NIR spectra, we have expanded the number of diagnostic lines sensitive to extinction, allowing us to investigate this interesting issue in more detail. For this purpose, we determined the extinction affecting the gas by comparing observed to predicted Case B recombination emission-line flux ratios, assuming the Cardelli et al. (1989) extinction law for $R_V = 3.1$. To obtain $E(B-V)$, we employed the fluxes $F_{\mathrm{Pa}\beta}$, $F_{\mathrm{Pa}\gamma}$, $F_{\mathrm{Pa}\delta}$ and $F_{\mathrm{Br}\gamma}$, which represent, respectively, the hydrogen line fluxes Paβ, Paγ, Paδ and Brγ. The expressions of Rodríguez-Ardila et al. (2017a) were employed for this purpose. In addition to these NIR H I lines, we also determined the extinction by means of the Balmer decrement Hα/Hβ in the optical region.

Finally, we also employed [Fe II] lines in the NIR to determine $E(B-V)$. This is because the transitions leading to the [Fe II] 1.257-μm and 1.644-μm lines originate from the same upper level. In the optical thin case, the ratio of their intrinsic line fluxes is simply given by the ratio of the corresponding spontaneous emission coefficients, which is constant and in principle known. Therefore, they are suitable diagnostics of extinction caused by dust due to the large wavelength separation between the lines. The intrinsic value of the ratio [Fe II] 1.257 μm/1.644 μm is estimated to be 1.25 with an uncertainty of 20 per cent (Bautista et al. 2015). In order to determine $E(B-V)$ using this ratio, we employed the expression derived by Rodríguez-Ardila et al. (2017a).

Riffel et al. (2006) and Rodríguez-Ardila et al. (2017a) have already shown that the ratio of the [Fe II] lines 1.257 μm/1.644 μm is in accordance with the extinction obtained using the Paβ/Brγ ratio and can be reliably applied to Seyfert 1 and 2 galaxies.

The values of $E(B-V)$ obtained using the five different dust-sensitive line ratios are listed in columns 2–6 of Table 2. Column 7 of the same table shows the final extinction for each galaxy, determined after averaging out the individual entries of the different indicators.

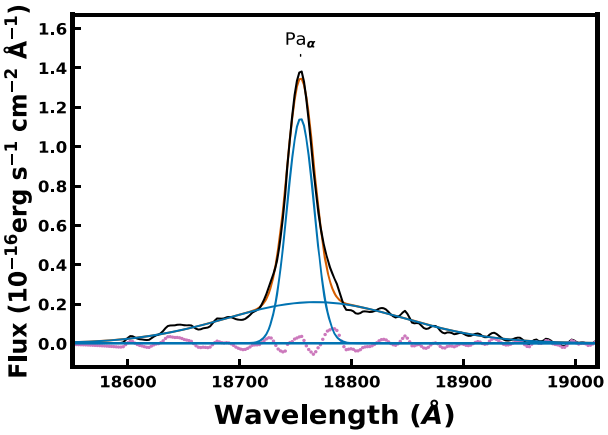

Figure 10. Same as Fig. 8 but for Paα in 2MASX J113111.05+162739.

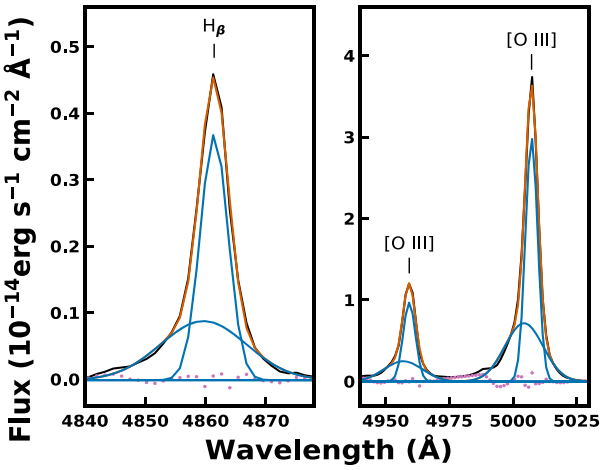

Figure 11. Same as Fig. 8 but for Hβ (left panel) and [O III] (right panel) observed in MRK 1388.

The overall very good match between $E(B-V)$ found from different indicators for the same galaxy indicates the consistency of our approach. Although some discrepancies are noted at some specific line ratios, differences of less than ∼0.3 mag between the minimum and maximum values of $E(B-V)$ were usually observed. We found that CLiF AGNs display extinction values similar to those found in samples of non-CLiF AGNs. For instance, Malkan et al. (2017) measured an average $E(B-V)$ of 0.49 ± 0.35 for type 1 and 0.52 ± 0.26 for type 2 Seyferts in their study of emission-line properties of Seyfert galaxies. They used a sample of 81 Seyfert 1 and 104 Seyfert 2 galaxies that comprise nearly all of the IRAS 12-μm AGN sample. Thus, in terms of intrinsic extinction, CLiF AGNs are similar to their non-CLiF counterparts.

Because all dust-sensitive NIR flux ratios employed here point towards small to moderate amounts of extinction, we conclude that the CLiF AGNs are affected, to some extent, by reddening in the nuclear region. Moreover, our values of the Hα/Hβ ratios were, in general, smaller than those of RET15 because of the subtraction of the stellar component. Indeed, the presence of the stellar population should affect the Balmer decrements, as the apertures employed to extract the spectra cover region sizes of the order of kiloparsecs.

This effect was already expected as the continuum emission displayed by the galaxies showed strong evidence of an underlying stellar population. In this scenario, Hβ tends to be more absorbed than Hα, increasing the flux ratio Hα/Hβ artificially. It is also worth mentioning that the values of $E(B-V)$ found here are low enough so that the Hγ/Hβ ratio is not significantly affected. It tends to be close to the theoretical value, as the separation in wavelength of the above two lines is small.

In Table 3 we list the Hα/Hβ ratios obtained by RET15 and the ratios we have obtained after removing the stellar population using pPXF. Because of the consistency of our results when using a larger number of diagnostic lines, throughout this work we consider that deviations from the intrinsic H I or [Fe II] 1.257 μm/1.644 μm ratios are due to extinction rather than to density effects. Thus, the emission-line fluxes for each galaxy were corrected by the corresponding $E(B-V)$ listed in the last column of Table 2.

4.3 Spectroscopic properties of CLiF AGNs and comparison with other AGNs

One of the most important characteristics of CLiF AGNs is the strength of the CLs, quantified by means of the emission-line flux ratios [Fe VII] λ6087/Hβ, [Fe X] λ6374/Hβ and [Ne V] λ3425/Hβ. In CLiF AGNs, the above ratios should be larger than 0.25, 0.2 and 1, respectively. In all cases, Hβ corresponds to the flux of the narrow component if the AGN is of Type I.

As shown in the previous section, Hβ may be strongly diluted by the presence of an underlying stellar population. Therefore, it is important to verify if the values of the above three line ratios still hold in CLiF AGNs after removing the stellar continuum. Moreover, if dust is present, correction by extinction will decrease [Fe VII] λ6087/Hβ and [Fe X] λ6374/Hβ and increase [Ne V] λ3425/Hβ.

Table 4 lists the line ratios between the most prominent CLs, normalized to the Hβ narrow component after subtraction of the stellar population and corrected by extinction. The flux values employed are listed in Tables A1–A6 in the online appendix. Overall, the derived ratios are close (within the uncertainties) to those defined by Rose et al. (2015a), which means that the limits established by them can be considered as guidelines to select sources with similar

Table 2. $E(B-V)$ (in mag) obtained for line ratios.

Galaxy	$E(B-V)_{\mathrm{Pa}\beta/\mathrm{Br}\gamma}$	$E(B-V)_{\mathrm{Pa}\gamma/\mathrm{Br}\gamma}$	$E(B-V)_{\mathrm{Pa}\delta/\mathrm{Br}\gamma}$	$E(B-V)_{[\mathrm{Fe\,II}]}$	$E(B-V)_{\mathrm{H}\alpha/\mathrm{H}\beta}$	$\langle E(B-V)\rangle$
ESO 138–G001	0.76 ± 0.12	0.47 ± 0.04	0.46 ± 0.03	0.68 ± 0.04	0.46 ± 0.01	0.57 ± 0.05
SDSS J164+43	–	–	–	–	0.22 ± 0.01	0.22 ± 0.01
III Zw 77	0.23 ± 0.06	0.52 ± 0.13	0.38 ± 0.06	1.16 ± 0.67[a]	0.17 ± 0.01	0.33 ± 0.05
MRK 1388	0.32 ± 0.26	0.10 ± 0.05	0.16 ± 0.06	0.00 ± 0.00	0.00 ± 0.00	0.12 ± 0.07
SDSS J124+44	–	–	–	–	0.27 ± 0.01	0.27 ± 0.01
NGC 424	0.27 ± 0.08	0.29 ± 0.06	0.13 ± 0.03	0.02 ± 0.01	0.45 ± 0.03	0.23 ± 0.04

[a] This value is not taken into account, on average.

Table 3. Comparison between values measured by RET15 (REF) and after the star population subtraction (Pop. Sub.) in our analysis.

Galaxy	$\langle E(B-V)\rangle$	Hα/H$\beta_{\rm REF}$	Hα/H$\beta_{\rm Pop.\ Sub.}$	Hγ/H$\beta_{\rm REF}$	Hγ/H$\beta_{\rm Pop.\ Sub.}$
ESO 138–G001	0.49 ± 0.05	4.25 ± 0.10	4.92 ± 0.05	0.48 ± 0.02	0.33 ± 0.01
SDSS J164+43	0.22 ± 0.01	5.38 ± 0.19	3.72 ± 0.43	0.40 ± 0.03	0.37 ± 0.06
III Zw 77	0.33 ± 0.05	4.15 ± 0.13	3.49 ± 0.39	0.34 ± 0.04	0.47 ± 0.09
MRK 1388	0.19 ± 0.05	3.95 ± 0.12	2.71 ± 0.90	0.49 ± 0.03	0.53 ± 0.03
SDSS J124+44	0.27 ± 0.01	6.36 ± 0.21	3.90 ± 0.35	0.47 ± 0.04	0.45 ± 0.11
2MASX J113+16	–	5.00 ± 0.17	–	5.00 ± 0.17	–
NGC 424	0.29 ± 0.03	5.77 ± 1.00	4.85 ± 0.37	0.48 ± 0.05	0.42 ± 0.04

Table 4. Most relevant optical line ratios that define a CLiF AGN after subtraction of the stellar population and correction by extinction.

Galaxy	[Ne V]/Hβ	[Fe VII]/Hβ	[Fe X]/Hβ
ESO 138–G001	0.58 ± 0.05	0.21 ± 0.01	0.07 ± 0.01
SDSS J164+43	5.13 ± 0.38	0.38 ± 0.07	0.11 ± 0.01
III Zw 77	–	0.16 ± 0.02	0.08 ± 0.01
MRK 1388	–	0.33 ± 0.01	0.14 ± 0.01
SDSS J124+44	–	0.54 ± 0.07	0.18 ± 0.04
NGC 424	1.96 ± 0.09	0.27 ± 0.04	0.08 ± 0.02

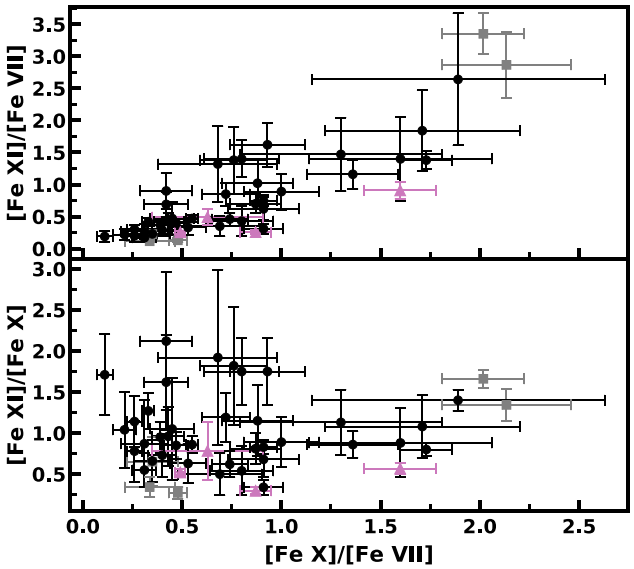

Figure 12. Observed [Fe XI]/[Fe VII] (top panel) and [Fe XI]/[Fe X] (bottom panel) versus [Fe X]/[Fe VII] ratios for the CLiF AGNs (magenta points). For comparison, the grey points are taken from Rodríguez-Ardila et al. (2006) and black points from Gelbord et al. (2009).

characteristics. However, in order to study the physical properties of these objects, the removal of the stellar continuum or the correction by reddening must be carried out first.

At this point, it is interesting to examine the relative strength of CLs in CLiF AGNs and to compare the results with values derived in the literature for other AGNs. For this purpose, we calculated the line flux ratios [Fe X] λ6374/[Fe VII] λ6087, [Fe XI] λ7890/[Fe X] λ6374 and [Fe XI] λ7890/[Fe VII] λ6087 in our sample of CLiF AGNs. Moreover, data from Rodríguez-Ardila et al. (2006) and Gelbord et al. (2009) were used for comparison purposes. We refer hereafter to the data taken from the literature as the comparison sample. For the present study, we included only galaxies that had a secure detection

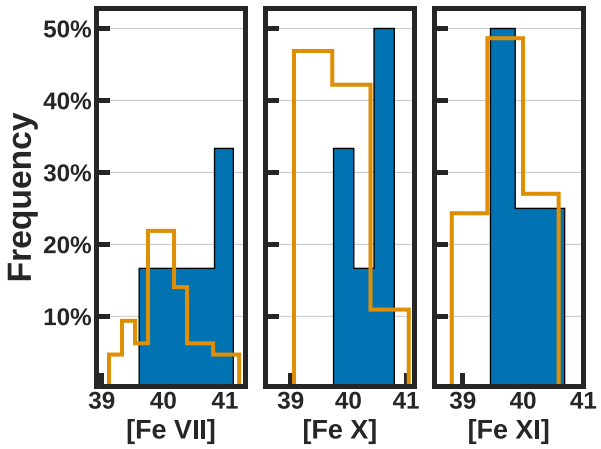

Figure 13. Histogram of luminosity values (log erg s^{-}1) for [Fe VII], [Fe X] and [Fe XI] for CLiF AGNs (in blue). For comparison, measures obtained by Gelbord et al. (2009) (in orange) were used.

in the above-mentioned three iron emission lines. This is because, in some cases, upper limits are driven by spurious residuals left after telluric correction or bad sky subtraction. Thus, to warrant meaningful values in the derived ratios, only fluxes detected at 3σ were employed. The results are shown in Fig. 12. It is important to highlight that Gelbord et al. (2009) selected the 63 AGNs of their sample based on the 3σ detection of the [Fe X] λ6374 line. Of these, 55 spectra included the spectral region containing [Fe XI] although it was detected (3σ) in only 37. Therefore, [Fe XI] was observed in 65 per cent of the sample. In our sample of CLiF AGNs, four objects included the region of [Fe XI] and in all of these that line was detected.

Fig. 12 shows that CLiF AGNs (full magenta triangles) and non-CLiF AGNs (full black circles and full grey squares) display similar values in the line ratio [Fe X]/[Fe VII], plotted on the x-axis of both panels. Likewise, the two ratios plotted on the y-axis, [Fe XI]/[Fe X] (bottom panel) and [Fe XI]/[Fe VII] (upper panel), are comparable in CLiF AGNs and non-CLiF AGNs. Under the assumption that the ratios depicted on the y-axis measure the ionization state of the CL gas, CLiF AGNs do not represent an extreme case within the AGN class. Therefore, we can safely state that when line flux ratios between optical CLs are considered, CLiF AGNs are not a separate class of AGNs.

We also derived the luminosity of the most prominent optical CLs in CLiF AGNs and compared these values to those found in the comparison sample. The results are shown in Fig. 13, where the luminosity distribution of [Fe VII] (left panel), [Fe X] (central panel) and [Fe XI] (right panel) is presented. The shaded blue histogram

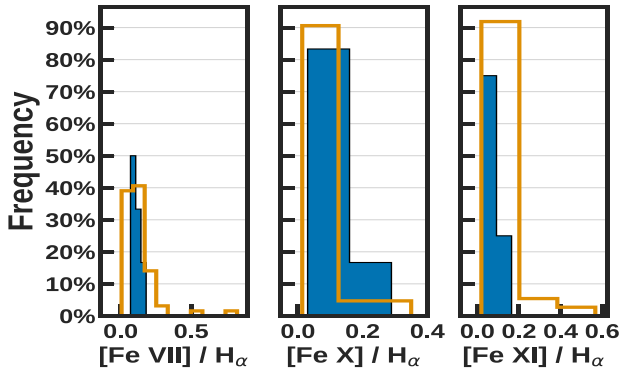

Figure 14. Histograms of the observed [Fe VII]/H_α, [Fe X]/H_α and [Fe XI]/H_α for the CLiF AGNs (in blue). For comparison, measures obtained by Gelbord et al. (2009) (in orange) were used. It is possible to verify that there is no great distinction between our sample and non-CLiF AGNs.

is for CLiF AGNs while the orange histogram represents non-CLiF AGNs. It can be seen that all three lines are distributed in a narrow interval of luminosity ($10^{39}-10^{41}$ erg s^{-1}) but CLiF AGNs tend to occupy the high end of the three distributions.

Moreover, we study the distribution of the ratios between CLs and H I lines for the above three iron lines in CLiF AGNs and non-CLiF AGNs. The main goal here is to compare if the values observed in the former are indeed extreme within the AGN class. The results, presented in Fig. 14, show precisely the opposite. The values of the ratios [Fe VII]/Hβ, [Fe X]/Hα and [Fe XI]/Hα found in CLiF AGNs are just part of a wider interval of values displayed by the comparison sample.

The availability of NIR spectra allowed us to study, for the first time in the literature, the spectroscopic properties of CLIF AGNs in this spectral region. Our main goal is to explore how these sources behave in the NIR when compared with non-CLiF AGNs.

A close examination of Figs 2–4 reveals that, in the NIR, optically classified CLiF AGNs display strong CLs of aluminium, calcium, iron, silicon and sulphur. A comparison of our sample spectra with the classical AGNs presented in Rodríguez-Ardila et al. (2011) shows the same ionization species. However, two important facts deserve mention here.

First, each CLiF AGN of this work displays all CLs already identified in previous samples in the interval 0.8–2.4 μm. In contrast, Rodríguez-Ardila et al. (2011) reported that it was in only three (NGC 1068 and 4051, and Ark 564) out of 54 AGNs that all CLs considered here were simultaneously detected. Moreover, they report that the four most prominent CLs in the NIR, [Si VI], [Si X], [S VIII] and [S IX], showed up all together in just 30 per cent of their sample. In a later work with a larger number of targets (104 AGNs), Lamperti et al. (2017) found that in just 18 per cent of their sample, more than two CLs were detected in the same spectrum. We ruled out sensitivity issues for the non-detection of CLs in most of the sources employed for comparison. However, in some cases, the spectral regions containing the lines are out of the filter bandpasses or severely affected by atmospheric transmission. In this work, the above four lines appeared in all six CLiF AGNs. Second, the [Fe XIII] doublet at 1.074, 1.0798 μm was detected in all CLiF AGNs here while it was identified in just 15 per cent of the non-CLiF AGN sample of Rodríguez-Ardila et al. (2011) and in 5 per cent of objects in Lamperti et al. (2017).

Following the optical analysis, we compare the relative intensity of CLs in CLiF AGNs to that of non-CLiF AGNs in the NIR. For this,

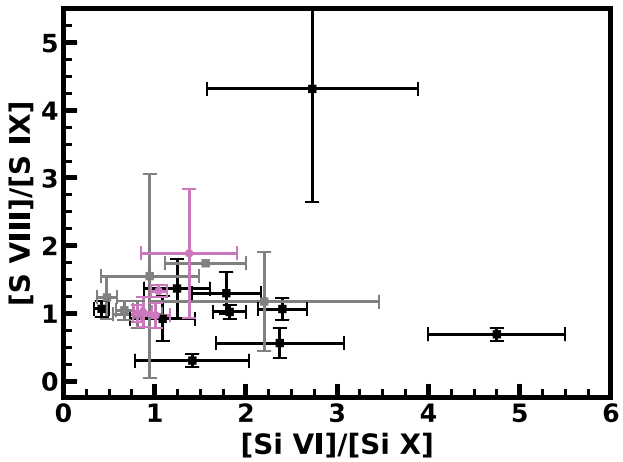

Figure 15. Observed [Si VI]/[Si X] versus [S VIII]/[S IX] ratios for the CLiF AGNs (magenta points). Black and grey points are for Type I and II AGNs, respectively, taken from Rodríguez-Ardila et al. (2011).

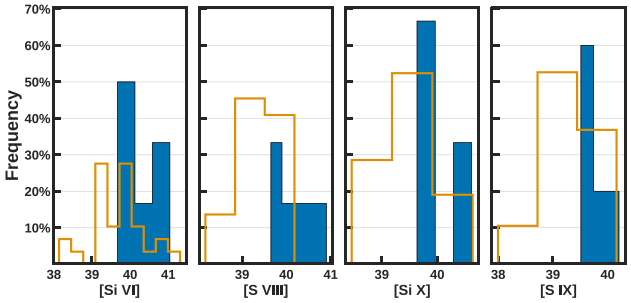

Figure 16. Histogram of the line luminosity distribution (log erg s^{-1}) for [Si VI], [S VII], [Si X] and [S IX] for CLiF AGNs (in blue). For comparison, data obtained by Rodríguez-Ardila et al. (2011) for non-CLiF AGNs (orange) were used.

we determined the line ratios [Si VI]/[Si X] and [S VIII]/[S IX] from the fluxes listed in Tables B1–B6 in the online appendix and we compare them with the values reported in Rodríguez-Ardila et al. (2011). Only 3σ detections were employed. Note that each ratio is independent of the gas metallicity. The results, shown in Fig. 15, suggest that CLiF AGNs have little scatter in both ratios, being concentrated mostly in the region with values of [Si VI]/[Si X] and [S VIII]/[S IX] of $\sim$1. The scatter observed in non-CLiF AGNs is indeed larger, with most points distributed in the intervals 0.3$-$2.2 and 0.2$-$2 for [Si VI]/[Si X] and [S VIII]/[S IX], respectively. From this comparison, we verify that, regarding CL ratios, no clear distinction between CLiF AGNs and non-CLiF AGNs is observed.

We also derive the luminosity of the above four NIR CLs and compare the distribution of values to that of non-CLiF AGNs. The results, shown in Fig. 16, confirm the trend already observed in the optical region. The values of CL luminosity in CLiF AGNs are preferentially located in the upper end of the distribution shown by non-CLiF AGNs. Indeed, CLiF AGNs occupy a very narrow range of values in luminosity: $10^{40}-10^{41}$ erg s^{-1} for [Si VI], [S VIII] and [Si X] and $\sim10^{39}-10^{40}$ erg s^{-1} for [S IX]. Non-CLiF AGNs stretch over a luminosity range of 2$-$3 dex, between 10^{39} and 10^{39} erg s^{-1}.

Finally, we also constructed the emission-line flux ratios [Si VI]/Brγ, [S VIII]/Paβ and [Si X]/Paβ to assess whether CLiF AGNs tend to display larger values in these ratios than in non-

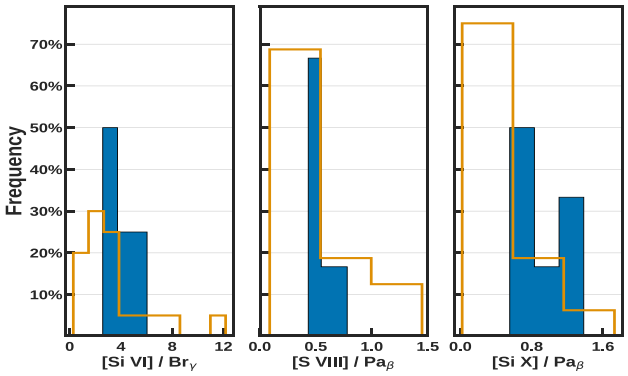

Figure 17. Histograms of the observed [Si VI]/Br$_\gamma$, [S VII]/Pa$_\beta$ and [Si X]/Pa$_\beta$ ratios for the CLiF AGNs (in blue) and non-CLiF AGNs (orange). Data for the later sample are from Rodríguez-Ardila et al. (2011).

CLiF AGNs. Fig. 17 shows the corresponding histograms. It can be easily seen that [Si VI] and [Si X] tend to be brighter relative to low-ionization lines in CLiF AGNs.

The results presented in the preceding paragraphs show that, regarding the relative strength of the most important CLs in the optical and NIR, CLiF AGNs are not distinguished among other AGNs. However, high-ionization lines in CLiF AGNs are usually confined to the upper-half of the luminosity distribution presented by AGNs in general. This tendency is also observed when ratios between CLs and H I lines are examined. CLiF AGNs tend to occupy the upper bins of the distributions when compared with the general AGN population. We are aware, though, that the small number of objects that comprise our CLiF AGN sample precludes a more conclusive statement. However, it is clear from our analysis that CLiF AGNs, by no means, represent a separate class of AGNs.

One possible scenario to enhance the high-ionization spectrum relative to that of a lower-ionization spectrum is to consider that the NLR is dominated by matter-bounded clouds. This hypothesis was proposed by Viegas & Prieto (1992) and Binette, Wilson & Storchi-Bergmann (1996) while trying to understand the nuclear and extended NLR emission of a sample of AGNs. They showed that the inclusion of photoionized matter-bounded clouds of sufficiently high excitation (high-ionization parameter) successfully reproduces the high-excitation lines. The low-excitation lines were accounted for by a population of low-ionization parameter, ionization-bounded clouds exposed to the ionizing radiation spectrum that leaks from the matter-bounded clouds. Variation of the relative proportion of the two types of clouds was found to have a similar effect on the combined emission-line spectrum to varying the ionization parameter in a traditional ionization parameter sequence.

This model was later applied by Binette et al. (1997) to the Circinus Galaxy, a Type II AGN widely known for its outstanding coronal emission-line spectrum. In order to explain the CLiF AGNs under this scenario, the number of matter-bounded clouds should largely exceed that of ionization-bounded clouds. Thus, the resulting spectrum is dominated by that emitted by the matter-bounded component. Although making a detail modelling of CLiF AGNs is out of the scope of this paper, in the next section we examine the physical properties of NLR gas. This will allow us to further constrain this scenario and to see whether it can be applied to our sample of AGNs.

Another mechanism that can enhance the high-ionization lines is shocks, driven by the interaction of a radio jet and the NLR gas or by nuclear outflowing material. The combined effect of nuclear photoionization and shocks strongly influences the strength of the CLs (Contini & Viegas 2001). This hypothesis was successfully applied to a local sample of AGNs in Rodríguez-Ardila et al. (2006), where evidence of high-ionization outflows was detected. According to the models of Contini & Viegas (2001), shock velocities of $V \geq 500$ km s^{-1} are necessary in order to produce very high ionization lines such as [Fe X] or [Si X]. Although the gas kinematics is discussed in Section 5, we anticipate that evidence of CL-driven shocks in the CLiF AGN sample exists but it cannot be applied to all targets studied here. For instance, broad components in the forbidden lines are observed in some of the sources, mainly in the [S III] line. In NGC 424, broad features are also observed in the CLs. However, in ESO 138–G001, Mrk 1388 and J124134.25+442639.2, no evidence of broad CLs was found. Although we do not discard the presence of shocks as an additional mechanism to enhance the CL emission, it is not be the main driver of the rich CL spectrum that characterizes CLiF AGNs.

At this point, we also highlight the identification of [S XII] 7611 Å, whose IP of 504.8 eV is the highest among all NIR and optical CLs examined here. Osterbrock (1981) had already noted the presence of an unidentified feature at 7613.1 ± 2.8 Å in III Zw 77 but he did not associate it with any particular emission line. Kraemer & Crenshaw (2000) were the first to attribute the line at 7611 Å detected in NGC 1068 to [S XII]. Here, we confirm the identification of [S XII] in III Zw 77 and MRK 1388. In the remaining CLiF AGNs, the region containing that feature is outside the spectral coverage of the data. Note that, to the best of our knowledge, [S XII] 7611 Å has been identified in just one extragalactic object. Therefore, we increased by a factor of 3 the number of sources where such a line is detected.

4.4 Physical conditions of the NLR in CLiF AGNs

In order to estimate the physical conditions of the NLR gas (electron density n_e and temperature T_e) several diagnostic line ratios were employed. Previously, all measured fluxes for the NLR were corrected for reddening, as derived in the previous section. The gas density was evaluated using two diagnostics: the [S II] 6716/6730 Å and [Ar IV] 4711/4740 Å emission-line flux ratios. The former is suitable for gas density below 10^4 cm^{-3} as the line ratio saturates when n_e is above that value. The latter is suitable for mapping gas of higher density ($<10^5$ cm^{-3}) because the lines involved have larger critical densities and IP than those of [S II]. Note that both diagnostics are insensitive to electron temperatures within a very large interval. In this calculation, we followed the procedure and relationships outlined in Proxauf, Oettl & Kimeswenger (2014), assuming always a temperature of 10^4 K. Varying the temperature by a factor of 3 up and down has very little effect on the results.

Electron temperatures were determined using single-ion emission pairs of lines that have excitation levels with a considerable difference in energy. A good example is the emission-line flux ratio [O III] (4959 + 5007)/4363 Å.

Other temperature-sensitive line ratios are [N II] (6548 + 6583)/5754 Å, [S II] (6716 + 6730)/4068 Å and [S III] (0.906 + 0.953) µm/6312 Å. The simultaneous detection of all these lines in the spectra of CLiF AGNs allowed us to compare the physical conditions resulting from different diagnostics. For [O III], we used the expressions derived by Proxauf et al. (2014) assuming an electron density of 10^4 cm^{-3}. The gas temperature from the three latter ratios we determined using the TEMDEN task included in the STSDAS version 3.18.3 package of IRAF. The results obtained from the electron density and temperature diagnostics are shown in Table 5.

Table 5. Density and temperature values for the NLR determined from sensitive emission-line flux ratios.

Galaxy	Density (cm^{-3})		Temperature (K)			
	[S II]	[Ar IV]	[O III]	[N II]	[S II]	[S III]
ESO 138–G001	449	3382	16 396	7490–10 074	4350–6133	Does not converge
SDSS J164+43	–	–	63 021	–	–	–
III Zw 77	384	–	33 620	11 539–18 097	4598–10 520	19 221–20 752
MRK 1388	964	16 753	–	13 187–22 055	6214	13 187–22 055
SDSS J124+44	652	–	Does not converge	–	–	–
NGC 424	542	2588	17 499	7773–10 563	3679–6215	–

Our results evidence n_e in the interval 10^2–10^4 cm^{-3}, in agreement with values found by other authors (Bennert et al. 2006; Kakkad et al. 2018) in samples with non-CLiF AGNs. This implies that the bulk of the NLR in CLiF AGNs is dominated by gas with density very similar to that found in other AGNs. The enhancement of CLs seen in these objects must be due to other physical properties.

Regarding the temperature, it can be verified that all values derived from [O III] suggest $T_e \sim 1.5{-}6 \times 10^4$ K. The other three sensitive temperature diagnostics show values in the interval $(1{-}2) \times 10^4$ K. This result further supports our hypothesis of a matter-bounded dominated NLR. According to Binette et al. (1997), the temperature in the matter-bounded clouds, where most of the [O III] and CLs would be produced, exceeds by at least 5000 K the temperature of ionization-bounded clouds, where the bulk of [N II], [S II] and other low-ionization species are produced. Moreover, according to Yan (2018), temperatures around 10^4 K are associated with the gas photoionized by the central source while values as large as 10^5 K are typically associated with the shocked gas. No evidence of such high T_e was found here. Thus, our results suggest that the NLR gas of CLiF AGNs is primarily photoionized by the AGNs although the presence of shocks is not discarded. Similar results were found by Rodríguez-Ardila et al. (2011) in the study of the CL region in a sample of non-CLiF AGNs.

We should note at this point that the physical conditions derived for the NLR can be extended to the CL region under the assumption that both regions share the same kinematics, chemical composition and physical extension, and are illuminated by the same ionizing continuum. Otherwise, our results here do not necessarily reflect the conditions of the gas producing the CLs. The lack of sensitive diagnostics of gas temperature involving high-ionization lines hinders the correct characterization of the CL region. In this regard, the observation of CLiF AGNs using adaptive optics (AO) and higher spectral resolution, at least for the closest sources, is fundamental to set firm constraints on the size and physical properties of the region emitting the CLs in these objects. Non-CLiF AGNs observed at spatial scales of ∼0.15 arcsec with AO systems and/or space-based observatories (i.e. the *Hubble Space Telescope*) show CL emission co-spatial with [O III], [S II] and H I gas in the inner portions of the NLR (Mazzalay et al. 2010; Müller-Sánchez et al. 2011; Rodríguez-Ardila et al. 2017b; May et al. 2018). These results warrant that, on a first approximation, the values of electron density and temperature derived for the NLR can be extended to the CL region.

5 KINEMATICS

5.1 Gas kinematics

Earlier studies using integrated long-slit spectroscopy found that CLs tend to be broader than forbidden low-ionization lines and their centroid position blueshifted relative to the systemic velocity of the galaxy (Wilson 1979; Pelat, Alloin & Fosbury 1981; Evans 1988). Furthermore, the presence of correlations between the width of the lines and the corresponding IP and/or critical density of the transitions were taken as evidence of a stratification in the ionization state of the gas, in the sense that the high-ionization gas would be located in the inner portions of the NLR with low-ionization gas farther out. The discovery of blue asymmetries, split line profiles and gas kinematics largely departing from rotation in the CLs suggested that at least part of the coronal gas is associated with outflowing material from the NLR (Erkens, Appenzeller & Wagner 1997; Rodríguez-Ardila et al. 2002, 2006; Müller-Sánchez et al. 2011; May et al. 2018).

However, not all AGNs with CLs display such extreme properties. Rodríguez-Ardila et al. (2011) found that the positive correlation between FWHM and IP was detected in 10 out of 54 galaxies examined. In some objects of their sample, no dependence at all between these two quantities was found while in some others, CLs have widths comparable to or even smaller than those displayed by low-ionization lines. Similar results were previously reported by Knop et al. (1996).

In CLiF AGNs, RET15 did not identify a correlation between FWHM and IP in any of the galaxies examined. In all cases, the distribution of FWHM values tends to be similar for low and high IP lines. Because of the availability of lines of higher IP in the NIR and the larger spectral resolution of our data compared with those of the SDSS, we revisited this issue.

Fig. 18 plots the FWHM versus IP for the seven CLiF AGNs of the sample. Even with the addition of new lines of high IP, there is no clear distinction between the FWHM of CLs and that of the low IP lines, confirming the previous results of RET15. Indeed, the distribution of values of FWHM found in CLiF AGNs is similar to that measured by Rodríguez-Ardila et al. (2011) for non-CLiF AGNs. Fig. 18 shows that NIR CLs display FWHM from 250 km s^{-1} (ESO 138–G001 and Mrk 1388) up to values larger than 1000 km s^{-1} (SDSS J164+43 and NGC 424). This same range in linewidth is also observed in low-ionization lines. This suggests that the velocity field of the NLR in CLiF AGNs and non-CLiF AGNs may be intrinsically the same.

Our data also confirm the lack of any trend between line shifts from the systemic velocity, ΔV, and the IP reported by RET15. Column 3 of Tables A1–A6 and B1–B6 lists ΔV (in km s^{-1}) for each emission line detected in the sample. It can be seen that the measured shift of the forbidden and permitted lines fluctuates regardless of the IP of the line. Also, no trend is detected between ΔV and FWHM.

Our results suggest that the region where the CLiF AGN is produced shares the same kinematics as the gas responsible for the emission of low-ionization lines. Under the assumption of a virialized velocity field and a stratification in the ionization state of the gas, in the sense that high-ionization lines would be produced closer to the central source (i.e. the torus) and lower-ionization lines outwards, we would expect a positive correlation between FWHM and IP, which is

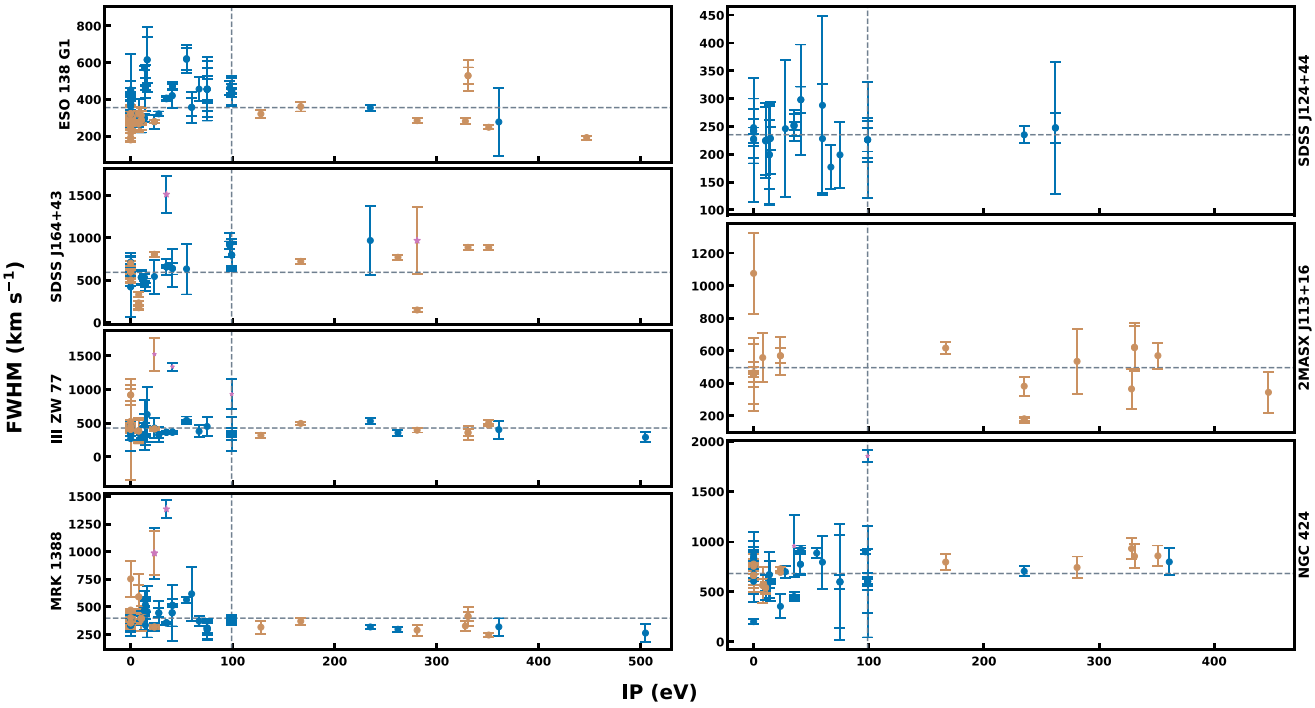

Figure 18. FWHM versus IP of the emission lines identified in the sample of CLiF AGNs. The blue dots represent the measurements for optical lines while brown dots are for NIR lines. The vertical dashed line represents the boundary for a line to be considered as coronal (IP $\geq$ 100 eV). The horizontal dashed line is the average value of the FWHM for each source.

not observed. The lack of such correlation, however, does not make CLiF AGNs special, as similar results were previously related in many other non-CLiF AGNs (Knop et al. 1996; Rodríguez-Ardila et al. 2011).

We highlight that extended emission from the NLR was not detected in any of the sources examined here. In all cases, the NLR was restricted to sizes <2 arcsec in the spatial direction of the slit. For the closest objects (ESO 138–G001, NGC 424, Mrk 1388 and III Zw 77), it translates to scales down to ∼400 pc. Therefore, the NLR of these objects should be very compact. If no stratification in gas ionization exists and the velocity field is not virialized, under seeing-limiting conditions, no correlation between FWHM and IP is expected. In order to confirm this scenario, we need observations of CLiF AGNs with telescopes equipped with AO systems that allow us to resolve angular scales down to tens of parsecs and at spectral resolutions of $R > 4000$. These data would allow us to put firm constraints on the kinematics and likely location of the CL region in such objects.

5.2 Stellar velocity dispersion and determination of black hole mass

Some of the spectroscopic properties displayed by CLiF AGNs can be explained if the mass of the central black hole is small ($M_{\rm BH} < 10^7$ M$_\odot$). Assuming that the CL region is photoionized by the continuum emitted primarily by the accretion disc, AGNs with smaller mass black holes will have hotter discs. In such a case, the peak of the spectral energy distribution is shifted towards higher energies. Under this scenario, CLs will be favoured because of the large supply of photons with energies in the X-ray domain. This idea was explored by Cann et al. (2018), who propose that intermediate mass black hole galaxies ($10^3 < M_{\rm BH} < 5 \times 10^6$) M$_\odot$ can be found by using the detection of bright CLs in the NIR and MIR region.

In this work, we determine $M_{\rm SMBH}$ from the stellar velocity dispersion σ_* obtained from the stellar population fit in the optical and NIR using pPXF. The relationship proposed by Kormendy & Ho (2013) was employed.

In order to measure σ_* in the NIR, we employed the Gemini NIR late-type stellar library (Winge, Riffel & Storchi-Bergmann 2009), which contains 60 individual stellar spectra with spectral types ranging from F7 III to M5 III, observed in the K band with a resolution of ∼3.2 Å (FWHM). For the optical spectra, the region containing the Ca II triplet was employed. In this case, we used the stellar templates of Cenarro et al. (2001), which contains 706 stellar spectra with 1.5 Å (FWHM) spectral resolution. These spectra are part of the medium-resolution Isaac Newton Telescope library (MILES; Sanchez-Blazquez et al. 2006).

The fits carried out with pPXF for the region of the CO and CaT absorption are shown in Figs 19 and 20, respectively. Table 6 displays σ obtained and the corresponding mass of the SMBH ($M_{\rm SMBH}$) for each galaxy. When two measurements of σ were available, we took the average of both values and the result was employed to determine $M_{\rm SMBH}$. From our sample of seven galaxies, we were able to measure the mass of the central black hole in six of them. Note that we do not employ the virial relationship because the strength of the broad component in Hβ or even in Hα was weak and this could introduce a bias in the $M_{\rm SMBH}$ determination.

Table 6 shows that CLiF AGNs display values of $M_{\rm SMBH}$ over a very narrow interval of $M_{\rm SMBH}$, between 10^7 and 10^8 M$_\odot$. NGC 3786, 4151 and 5548 are among bona-fide Type I AGNs with $M_{\rm SMBH}$ in the above range (Bentz & Katz 2015). They display a very rich CL spectrum, in both the optical and the NIR (Evans 1988; Knop et al. 1996; Rodríguez-Ardila et al. 2011). Therefore, the CLiF nature of

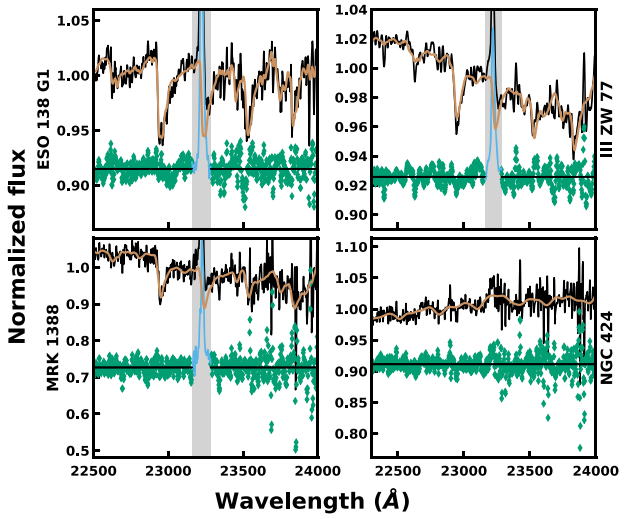

Figure 19. Fit of pPXF to the region around the 2.32-μm CO absorptions. The black line is the observed spectrum while the brown line is the best fit. Regions masked from the fit are in blue and residuals are in green.

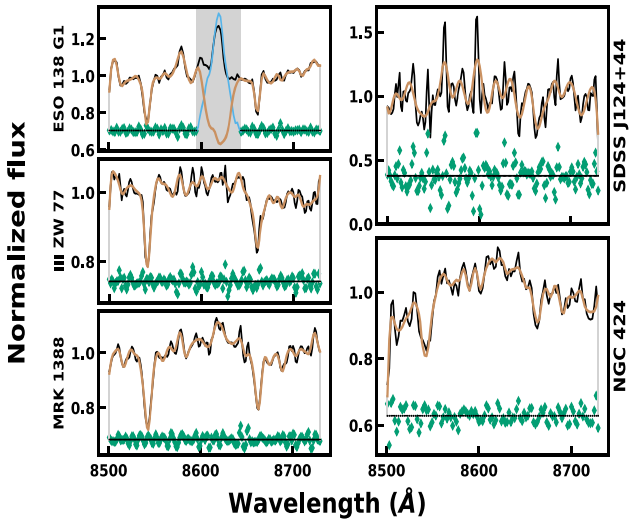

Figure 20. The same as Fig. 19 but for the region around the CaT absorptions.

our sources cannot be ascribed to a mere effect of the central black hole mass. It is certainly worth exploring other properties, such as bolometric luminosity, Eddington ratio and accretion rate, for CLiF and non-CLiF sources in order to detect any trend that could explain the peculiar properties of the former. We leave this analysis for future work as it is first mandatory to expand the number of sources with CLiF properties for meaningful statistics.

6 FINAL REMARKS

In the contemporary scenario, the study of forbidden high-ionization lines in AGNs is of great importance in order to gather crucial insights about the most energetic processes in the inner portion of the NLR. Here, we have carried out a multiwavelength analysis of a selected group of AGNs known to display a prominent CLiF spectrum. In addition to optical data, we include the first report of NIR spectroscopy on these objects in the literature. The combination of optical and NIR spectroscopy aims to improve our understanding of the physical processes at work in the central parsecs of these objects and to unveil whether CLiF AGNs are indeed a special class of AGNs. The main results gathered from this work are summarized as follows.

(i) The optical and NIR continuum emission in CLiF AGNs observed under seeing-limited conditions is strongly affected by the underlying stellar population of the host galaxy. Thus, in order to study the gas emission, it is first necessary to model and subtract that component. In the NIR, in addition to the stellar contribution, a continuum emission due to dust heated at temperatures between 700 and 1500 K by the AGN is also present. It dominates the *H*-band continuum and redwards.

(ii) The analysis of the emission-line spectrum showed the presence of broad components with FWHM $\geq$ 2000 km s^{-1} in the permitted lines in three out of four galaxies previously classified as Type II AGNs. This result points out that the sample of CLiF AGNs is dominated by Type I objects instead of Type II.

(iii) Because of the increase in wavelength coverage by including NIR spectra, we employed five different diagnostics of extinction to assess if dust is present in the NLR. We found that CLiF AGNs are affected by reddening in the nuclear region, with values in the range $0.12 \leq E(B-V) \leq 0.57$. In this determination, the subtraction of the stellar population proved to be critical, as Hβ may be strongly diluted by the presence of that component.

(iv) We derived the emission-line flux ratios [Fe XI] λ7890/[Fe X] λ6374 and [Fe X] λ6374/[Fe VII] λ6087 in the optical and [Si VI] 1.963 μm/[Si X] 1.43 μm and [S VIII] 0.991 μm/[S IX] 1.251 μm in the NIR for the CliF AGNs. They were compared with those measured in normal AGNs with CL emission. The analysis showed that the two groups of AGNs are not distinguished regarding the relative strength of these CLs. However, it is interesting to note that CLiF AGNs display simultaneously all CLs previously identified in other AGNs. This strongly contrasts with what is found in samples of non-CLiF AGNs, where less than 5 per cent of the galaxies display lines such as [Fe XIII] or [S XI]. Moreover, CLiF AGNs display a conspicuous forest of [Fe V], [Fe VI] and [Fe VII] lines in the optical region, rarely seen in classical AGNs.

(v) The remarkable CL spectrum displayed by CLiF AGNs and their strong intensity relative to low-ionization lines suggests that these sources have an NLR dominated by matter-bounded clouds. Such clouds are responsible for the emission of high-excitation lines. Ionization-bounded clouds, where the low-ionization lines are emitted, should be outnumbered by the former.

(vi) Temperature and density diagnostics were employed to characterize the physical state of the NLR in the CLiF AGN sample. We found values of T_e in the range $10^4-6.3 \times 10^4$ K, measured from the [O III] and [S III] lines. Temperature diagnostics using low-ionization lines ([N II] and [S II]) suggest smaller T_e of $\sim 10^4$ K. This result further supports our hypothesis of a matter-bounded dominated NLR. Values of gas density (n_e) using sulphur and argon lines indicate values close to 500 cm^{-3} and up to 1.6×10^4 cm^{-3}, respectively. Overall, the NLR ionization mechanism is associated with photoionization by the central source although the presence of shocks is not fully discarded.

(vii) The kinematics of the NLR show that the CL gas shares similar characteristics to that emitting low-ionization lines. For instance, no trend between FWHM and IP is observed, even after considering several lines with IP >100 eV and up to ∼500 eV. Thus, it is not possible to assess if the gas responsible for the coronal emission is located in the inner portion of the NLR. However, the lack of extended NLR emission in all CLiF AGNs suggests that

Table 6. Values of σ in units of km s^{-1} and the values obtained for the masses of the SMBHs ($M_\odot$) by means of the M–σ ratio (Kormendy & Ho 2013).

Galaxy	σ_{CO}	σ_{CaT}	σ	M_{SMBH}
ESO 138–G001	124.90 ± 7.01	131.03 ± 14.30	127.96 ± 7.96	$4.37^{+1.14}_{-1.02} \times 10^7$
SDSS J164+43	–	–	–	$2.7 \pm 0.4 \times 10^7$ [a]
III Zw 77	166.99 ± 14.72	161.59 ± 10.17	164.29 ± 12.44	$1.31^{+0.11}_{-0.10} \times 10^8$
MRK 1388	160.41 ± 20.55 [b]	112.95 ± 8.30	112.95 ± 8.30	$2.53^{+1.14}_{-1.02} \times 10^7$
SDSS J124+44	–	119.97 ± 18.43	119.97 ± 18.43	$3.29^{+1.15}_{-1.02} \times 10^7$
NGC 424	–	146.65 ± 12.76	146.65 ± 12.76	$7.94^{+1.14}_{-1.02} \times 10^7$

[a] For this object, it is not possible to identify stellar absorption signatures. The power law that describes the AGN emission has a greater influence on the continuum (see Figs 5 and 6). Thus, we employed the virial relation of Vestergaard & Peterson (2006), which relates the black hole mass to the brightness of the AGN emission continuum at 5100 Å and the width of the BLR hydrogen lines.
[b] As can be seen in Fig. 19, the K-band spectrum does not have well-defined CO absorptions, so this value was not used in the analysis.

the bulk of the NLR gas is nuclear, and subjected to our angular resolution, presumably within the inner 500 pc.

(viii) We determined the mass of the SMBH, using the M–σ relationship and the virial scaling using the FWHM of Hβ and the continuum luminosity at 5100 Å. All masses were found to be in a very narrow range of values, between 10^7 and 10^8 $M_\odot$. This result rules out the hypothesis that the CLiF AGNs are due to a very hot accretion disc (i.e. that produced by a small black hole mass AGN).

We conclude that CLiF AGNs are not a separate class of AGNs due to the enhancement of the forbidden high-ionization line spectrum. However, when compared with non-CLiF AGNs, they usually occupy the high end of the distribution either in CL luminosity or when a line flux ratio between a given CL and H I lines is considered. It is fundamental to identify a larger number of sources with similar characteristics to elaborate more definitive conclusions about the properties of the NLR in these objects. Moreover, observations of existing sources, at least the closest ones, at larger angular resolutions will strongly help to put firm constraints on the size of the NLR and of the CL region.

ACKNOWLEDGEMENTS

We thank the anonymous referee for useful comments and suggestions that have improved the manuscript. FCCC acknowledges a PhD grant from CAPES. RR thanks CNPq, CAPES and FAPERGS for partially funding this project. ARA acknowledges CNPq for partial support of this project. Based on observations obtained at the Gemini Observatory, which is operated by the Association of Universities for Research in Astronomy, Inc., under a cooperative agreement with the National Science Foundation (NSF) on behalf of the Gemini partnership: the NSF (United States), National Research Council (Canada), CONICYT (Chile), Ministerio de Ciencia, Tecnología e Innovación Productiva (Argentina), Ministério da Ciência, Tecnologia e Inovações (Brazil), and Korea Astronomy and Space Science Institute (Republic of Korea). This paper is also based on observations obtained at the Southern Astrophysical Research (SOAR) telescope, which is a joint project of the Ministério da Ciência, Tecnologia, Inovações e Comunicações (MCTIC) do Brasil, the US National Optical Astronomy Observatory (NOAO), the University of North Carolina at Chapel Hill (UNC), and Michigan State University (MSU).

DATA AVAILABILITY

The data underlying this article will be shared on reasonable request to the corresponding author.

REFERENCES

Abazajian K. N. et al., 2009, ApJS, 182, 543
Baldwin J., Stone R. P., 1984, MNRAS, 206, 241
Barvainis R., 1987, ApJ, 320, 537
Bautista M. A., Fivet V., Ballance C., Quinet P., Ferland G., Mendoza C., Kallman T. R., 2015, ApJ, 808, 174
Bennert N., Jungwiert B., Komossa S., Haas M., Chini R., 2006, A&A, 446, 919
Bentz M. C., Katz S., 2015, PASP, 127, 67
Binette L., Wilson A. S., Storchi-Bergmann T., 1996, A&A, 312, 365
Binette L., Wilson A. S., Raga A., Storchi-Bergmann T., 1997, A&A, 327, 909
Bruzual G., Charlot S., 2003, MNRAS, 344, 1000
Cann J. M., Satyapal S., Abel N. P., Ricci C., Secrest N. J., Blecha L., Gliozzi M., 2018, ApJ, 861, 142
Cappellari M., 2017, MNRAS, 466, 798
Cappellari M., Emsellem E., 2004, PASP, 116, 138
Cardelli J. A., Clayton G. C., Mathis J. S., 1989, ApJ, 345, 245
Cenarro A., Cardiel N., Gorgas J., Peletier R., Vazdekis A., Prada F., 2001, MNRAS, 326, 959
Clemens J. C., Crain J. A., Anderson R., 2004, in Moorwood A. F. M., Iye M., eds, Proc. SPIE Conf. Ser. Vol. 5492, Ground-based Instrumentation for Astronomy, SPIE, Bellingham, p. 331
Contini M., Viegas S., 2001, ApJS, 132, 211
Cushing M. C., Vacca W. D., Rayner J. T., 2004, PASP, 116, 362
Denney K. et al., 2014, ApJ, 796, 134
Doi A., 2015, PASJ, 67, 15
Dopita M. A., Vogt F. P., Sutherland R. S., Seitenzahl I. R., Ruiter A. J., Ghavamian P., 2018, ApJS, 237, 10
Edelson R., Malkan M., 1986, ApJ, 308, 59
Elias J. H., Rodgers B., Joyce R. R., Lazo M., Doppmann G., Winge C., Rodríguez-Ardila A., 2006, in McLean I. S., Iye M., eds, Proc. SPIE Conf. Ser. Vol. 6269, Ground-based and Airborne Instrumentation for Astronomy. SPIE, Bellingham, p. 626914
Erkens U., Appenzeller I., Wagner S., 1997, A&A, 323, 707
Evans I., 1988, ApJS, 67, 373
Gelbord J. M., Mullaney J. R., Ward M. J., 2009, MNRAS, 397, 172
Glidden A., Rose M., Elvis M., McDowell J., 2016, ApJ, 824, 34
Goulding A., Alexander D., 2009, MNRAS, 398, 1165
Kakkad D. et al., 2018, A&A, 618, A6
Knop R., Armus L., Larkin J., Matthews K., Shupe D., Soifer B., 1996, AJ, 112, 81

Kollatschny W., Fricke K., 1985, A&A, 146, L11
Komossa S. et al., 2008, ApJ, 678, L13
Komossa S. et al., 2009, ApJ, 701, 105
Kormendy J., Ho L. C., 2013, ARA&A, 51, 511
Kraemer S. B., Crenshaw D. M., 2000, ApJ, 532, 256
Lamperti I. et al., 2017, MNRAS, 467, 540
Landt H., Ward M. J., Steenbrugge K. C., Ferland G. J., 2015a, MNRAS, 449, 3795
Landt H., Ward M. J., Steenbrugge K. C., Ferland G. J., 2015b, MNRAS, 454, 3688
Lyutyj V., Oknyanskij V., Chuvaev K., 1984, Soviet Astronomy Letters, 10, 335
Malkan M. A., Jensen L. D., Rodriguez D. R., Spinoglio L., Rush B., 2017, ApJ, 846, 102
Mason R. E. et al., 2015, ApJS, 217, 13
May D., Rodríguez-Ardila A., Prieto M., Fernández-Ontiveros J., Diaz Y., Mazzalay X., 2018, MNRAS, 481, L105
Mazzalay X., Rodríguez-Ardila A., Komossa S., 2010, MNRAS, 405, 1315
Murayama T., Taniguchi Y., 1998, ApJ, 503, L115
Müller-Sánchez F., Prieto M., Hicks E., Vives-Arias H., Davies R., Malkan M., Tacconi L., Genzel R., 2011, ApJ, 739, 69
Newville M., Stensitzki T., Allen D. B., Rawlik M., Ingargiola A., Nelson A., 2016, Astrophysics Source Code Library, record ascl:1606.014
Oknyansky V., Winkler H., Tsygankov S., Lipunov V., Gorbovskoy E., van Wyk F., Buckley D., Tyurina N., 2019, MNRAS, 483, 558
Oliva E., Moorwood A., Drapatz S., Lutz D., Sturm E., 1999, preprint (arXiv: astro-ph/9901254)
Osterbrock D., 1981, ApJ, 246, 696
Osterbrock D. E., Ferland G. J., 2006, Astrophysics of Gas Nebulae and Active Galactic Nuclei. University Science Books, Mill Valley, CA
Pecaut M. J., Mamajek E. E., 2013, ApJS, 208, 9
Pelat D., Alloin D., Fosbury R. A., 1981, MNRAS, 195, 787
Penston M., Fosbury R., Boksenberg A., Ward M., Wilson A., 1984, MNRAS, 208, 347
Pogge R. W., Owen J., 1993, Ohio State Univ. Internal Report No. 93-01
Pottasch S., Bernard-Salas J., Roellig T., 2009, A&A, 499, 249
Prieto M. A., Viegas S. M., 2000, ApJ, 532, 238
Prieto M. A., García A. P., Espinosa J. R., 2002, MNRAS, 329, 309
Prieto M., Marco O., Gallimore J., 2005, MNRAS, 364, L28
Proxauf B., Oettl S., Kimeswenger S., 2014, A&A, 561, A10
Rayner J., Toomey D., Onaka P., Denault A., Stahlberger W., Vacca W., Cushing M., Wang S., 2003, PASP, 115, 362
Rayner J. T., Cushing M. C., Vacca W. D., 2009, ApJS, 185, 289
Reunanen J., Kotilainen J., Prieto M., 2003, MNRAS, 343, 192
Riffel R., Rodríguez-Ardila A., Pastoriza M. G., 2006, A&A, 457, 61
Riffel R., Pastoriza M. G., Rodríguez-Ardila A., Bonatto C., 2009, MNRAS, 400, 273
Rodríguez-Ardila A., Mazzalay X., 2006, MNRAS, 367, L57
Rodríguez-Ardila A., Viegas S. M., Pastoriza M. G., Prato L., 2002, ApJ, 579, 214
Rodríguez-Ardila A., Prieto M. A., Viegas S., Gruenwald R., 2006, ApJ, 653, 1098
Rodríguez-Ardila A., Prieto M., Portilla J., Tejeiro J., 2011, ApJ, 743, 100
Rodríguez-Ardila A. et al., 2017a, MNRAS, 465, 906
Rodríguez-Ardila A., Prieto M., Mazzalay X., Fernández-Ontiveros J., Luque R., Müller-Sánchez F., 2017b, MNRAS, 470, 2845
Rose M., Elvis M., Tadhunter C. N., 2015a, MNRAS, 448, 2900
Rose M., Elvis M., Crenshaw M., Glidden A., 2015b, MNRAS, 451, L11
Sanchez-Blazquez P. et al., 2006, MNRAS, 371, 703
Satyapal S., Vega D., Dudik R. P., Abel N. P., Heckman T., 2008, ApJ, 677, 926
Schaerer D., Stasinska G., 1999, preprint (arXiv:astro-ph/9903430)
Schlafly E. F., Finkbeiner D. P., 2011, ApJ, 737, 103
Schlawin E. et al., 2014, in Ramsay S. K., McLean I. S., Takami H., eds, Proc. SPIE Conf. Ser. Vol. 9147, Ground-based and Airborne Instrumentation for Astronomy V. SPIE, Bellingham, p. 91472H
Skrutskie M. et al., 2006, AJ, 131, 1163
Smith N. et al., 2009, ApJ, 695, 1334
Vacca W. D., Cushing M. C., Rayner J. T., 2003, PASP, 115, 389
Vestergaard M., Peterson B. M., 2006, ApJ, 641, 689
Viegas S. M., Prieto M. A., 1992, MNRAS, 258, 483
Wang T-G., Zhou H-Y., Wang L-F., Lu H-L., Xu D., 2011, ApJ, 740, 85
Wilson A., 1979, Proc. R. Soc. Lond. A, 366, 461
Winge C., Riffel R. A., Storchi-Bergmann T., 2009, ApJS, 185, 186
Yan R., 2018, MNRAS, 481, 476

SUPPORTING INFORMATION

Supplementary data are available at *MNRAS* online.

APPENDIX A: OPTICAL EMISSION-LINE TABLES
APPENDIX B: NEAR-INFRARED EMISSION-LINE TABLES

Please note: Oxford University Press is not responsible for the content or functionality of any supporting materials supplied by the authors. Any queries (other than missing material) should be directed to the corresponding author for the article.

This paper has been typeset from a TEX/LATEX file prepared by the author.